REPORT DOCUMENTATION PAGE

Form Approved OMB NO. 0704-0188

1. REPORT DATE (DD-MM-YYYY) 09-07-2019	2. REPORT TYPE Final Report	3. DATES COVERED (From - To) 1-Sep-2015 - 31-Mar-2019

4. TITLE AND SUBTITLE
Final Report: Generation and frequency conversion of quantum states in high "Q" SRF parametric oscillators

5a. CONTRACT NUMBER
W911NF-15-1-0557

5b. GRANT NUMBER

5c. PROGRAM ELEMENT NUMBER

6. AUTHORS

5d. PROJECT NUMBER

5e. TASK NUMBER

5f. WORK UNIT NUMBER

7. PERFORMING ORGANIZATION NAMES AND ADDRESSES
University of California - Merced
5200 North Lake Road

Merced, CA 95343 -5705

8. PERFORMING ORGANIZATION REPORT NUMBER

9. SPONSORING/MONITORING AGENCY NAME(S) AND ADDRESS (ES)
U.S. Army Research Office
P.O. Box 12211
Research Triangle Park, NC 27709-2211

10. SPONSOR/MONITOR'S ACRONYM(S)
ARO

11. SPONSOR/MONITOR'S REPORT NUMBER(S)
68066-PH-DRP.4

12. DISTRIBUTION AVAILIBILITY STATEMENT
Approved for public release; distribution is unlimited.

13. SUPPLEMENTARY NOTES
The views, opinions and/or findings contained in this report are those of the author(s) and should not contrued as an official Department of the Army position, policy or decision, unless so designated by other documentation.

14. ABSTRACT

15. SUBJECT TERMS

16. SECURITY CLASSIFICATION OF:			17. LIMITATION OF ABSTRACT	15. NUMBER OF PAGES	19a. NAME OF RESPONSIBLE PERSON
a. REPORT	b. ABSTRACT	c. THIS PAGE			Jay Sharping
UU	UU	UU	UU		19b. TELEPHONE NUMBER 209-228-4049

Standard Form 298 (Rev 8/98)
Prescribed by ANSI Std. Z39.18

RPPR Final Report
as of 29-Aug-2019

Agency Code:

Proposal Number: 68066PHDRP **Agreement Number: W911NF-15-1-0557**

INVESTIGATOR(S):

Name: Jay Edward Sharping
Email: jsharping@ucmerced.edu
Phone Number: 2092284049
Principal: Y

Organization: **University of California - Merced**
Address: 5200 North Lake Road, Merced, CA 953435705
Country: USA

DUNS Number: 113645084 EIN: 943067788
Report Date: 30-Jun-2019 Date Received: 09-Jul-2019
Final Report for Period Beginning 01-Sep-2015 and Ending 31-Mar-2019
Title: Generation and frequency conversion of quantum states in high "Q" SRF parametric oscillators
Begin Performance Period: 01-Sep-2015 **End Performance Period:** 31-Mar-2019
Report Term: 0-Other
Submitted By: Jay Sharping Email: jsharping@ucmerced.edu
Phone: (209) 228-4049
Distribution Statement: 1-Approved for public release; distribution is unlimited.

STEM Degrees: 1 **STEM Participants:** 4

Major Goals: Phase I is an 18-month effort with a budget of $200,000 to evaluate the expected performance of such a scheme and to demonstrate squeezing of RF fields.
The key tasks are:
1) Quantify the oscillation threshold for a degenerate parametric oscillator in terms of cavity Q, and frequency of operation.
2) Quantify the fundamental and practical limits to squeezing in such a device.
3) Determine the merits and drawbacks of quadrature squeezing in a degenerate scheme vs. two-mode squeezing in a nondegenerate scheme.
4) Implement an experimental apparatus for squeezing generation at microwave frequencies.
5) Implement an experimental apparatus for squeezing measurements at microwave frequencies.
6) Quantify the fundamental and practical limits associated with the fidelity of transferring the squeezed state from microwave to optical frequencies.
The 6 tasks listed above fall into 3 categories: 1) SRF cavity design, fabrication and test (we will build one prototype and then a second SRF cavity); 2) measurement apparatus design, implementation and test; and 3) theoretical support.

Phase II is an additional 18-month effort with a budget of $200,000 to demonstrate the frequency conversion of squeezed RF fields to optical frequencies. The key tasks are:
1) Implement optical input/output access to the dilution refrigerator and implement an optical channel for Doppler shifting of the optical field in the presence of the moving SRF cavity membrane.
2) Implement and test the optical squeezing characterization circuit.
3) Quantify the efficiency of squeezing translation in such a device.

Accomplishments: II-A Normal mode splitting in coupled SRF cavities
Three-dimensional radio frequency cavities demonstrate excellent frequency selectivity and, as such, are known for their use in RF filters. These cavities have potential applications in quantum information science, precision displacement metrology, and quantum electrodynamics. Additionally, coupled cavities that form a spectral doublet allow for parametric gain when incorporating mechanical elements. Here, we investigate normal-mode splitting in a pair of quarter-wave stub microwave cavities at room temperature and cryogenic environments in order to identify coupling mechanics for normal and superconducting systems. Superconducting quarter-wave stub cavities with a resonant frequency of 10 GHz are made from reactor-grade niobium and exhibit Q ranging from 105 to 109. We varied coupling from the weak coupling regime to the strong coupling regime. The minimum observed doublet

separation was 7 MHz for room temperature tests and 200 kHz for cryogenic tests. We also report on values of intrinsic quality factor for the tuning cavity as a dielectric rod is translated along its symmetry axis. The realization of coupled superconducting radio-frequency cavities of this type is a necessary step towards implementation of parametric SRF-mechanical gain.
See full paper in the "Upload" section.

II-B Electrostatic tuning of SRF cavities
We implement a non-contact, external method of simultaneously fine-tuning a mechanical resonator and a superconducting radio frequency (SRF) cavity using a capacitor formed between a silicon nitride membrane and a copper electrode at cryogenic temperatures. The silicon nitride membrane forms a variable boundary condition for the SRF cavity thereby creating the optomechanical cavity. By controlling the DC voltage applied between an external electrode and the silicon nitride membrane we are capable of tuning the resonance frequency internal to the SRF cavity up to 25 kHz for a cavity with loaded quality factor of 2.5 million, corresponding to six cavity linewidths. At the same time we observe the electrostatic frequency shift of the membrane. This approach has the unique benefit of avoiding any dielectric insertion or added gaps due to a moving end-wall thereby limiting the loss of the cavity. Furthermore, this design avoids applied pressure typically used with piezoelectric devices in accelerator cavities. This work seeks to have strong impact in tuning high-Q cavities due to its ability to maintain low losses.
See full paper in the "Upload" section.

II-C Electromagnetic coupling to centimeter-scale mechanical membrane resonators via RF cylindrical cavities
We present experimental and theoretical results for the excitation of a mechanical oscillator via radiation pressure with a room-temperature system employing a relatively low-(Q) centimeter-size mechanical oscillator coupled to a relatively low-Q standard three-dimensional radio-frequency (RF) cavity resonator. We describe the forces giving rise to optomechanical coupling using the Maxwell stress tensor and show that nanometer-scale displacements are possible and experimentally observable. The experimental system is composed of a 35mmdiameter silicon nitride membrane sputtered with a 300 nm gold conducting film and attached to the end of a RF copper cylindrical cavity. The RF cavity is operated in its TE011mode and amplitude modulated on resonance with the fundamental drum modes of the membrane. Membrane motion is monitored using an unbalanced, non-zero optical path difference, optically filtered Michelson interferometer capable of measuring sub-nanometer displacements.
See full paper in the "Upload" section.

II-D Simulation analysis of practical cavity designs
In this paper we report on designs, simulations and experiments with two types of high-Q 3- dimensional cavities: cylindrical TE011, and coaxial quarter-wave stub. We investigate the dependence of Q on the practical implementation tolerances of gaps between components, shape imperfections, and frequency tuning strategies. We find that cylindrical cavities can maintain high Q for designs which include frequency tunability and mechanical oscillators as long as extraordinary care is taken with shape and gap tolerance during construction and assembly. Coaxial stub cavities can be made frequency tunable while maintaining high Q, but require more creativity to include a mechanical element. Finally, we report on a coaxial stub cavity incorporating a conically-shaped stub which confines the electric field near the stub's tip stub, thus enhancing field-matter interactions near the tip.
See full paper in the "Upload" section.

II-E A parametric oscillator for classroom demonstration or student laboratory
We describe a simple and intuitive parametric oscillator apparatus which is suitable for a classroom demonstration or an upper division laboratory. In order to facilitate the incorporation of this apparatus into the physics curriculum, we provide the learning objectives for an upper-division physics laboratory experiment. We present typical experimental data illustrating the main features of parametric oscillators including oscillation threshold, frequency shifting at large amplitude and bistability. Our experiments and theory emphasize identifying the lowest-order threshold for oscillation in terms of the modulation depth and quality factor. This experiment provides a foundation for understanding current research such as that in quantum opto-mechanics and nonlinear dynamics.
See full paper in the "Upload" section.

Training Opportunities: Graduate students Johnathon Thompson, Alessandro Castelli and Jacob Pate were partially supported during their PhD programs.

Postdoctoral associate Luis A. Martinez had projects which were partially supported during this program.

Results Dissemination: Papers are summarized in the "Accomplished" section and attached in the "Upload" section.

Honors and Awards: Nothing to Report

Protocol Activity Status:

Technology Transfer: Nothing to Report

PARTICIPANTS:

Participant Type: PD/PI
Participant: Jay E Sharping
Person Months Worked: 1.00 **Funding Support:**
Project Contribution:
International Collaboration:
International Travel:
National Academy Member: N
Other Collaborators:

Participant Type: Graduate Student (research assistant)
Participant: Alessandro Castelli
Person Months Worked: 6.00 **Funding Support:**
Project Contribution:
International Collaboration:
International Travel:
National Academy Member: N
Other Collaborators:

Participant Type: Graduate Student (research assistant)
Participant: Jacob Pate
Person Months Worked: 12.00 **Funding Support:**
Project Contribution:
International Collaboration:
International Travel:
National Academy Member: N
Other Collaborators:

Participant Type: Graduate Student (research assistant)
Participant: Johnathon Thompson
Person Months Worked: 12.00 **Funding Support:**
Project Contribution:
International Collaboration:
International Travel:
National Academy Member: N
Other Collaborators:

ARTICLES:

Publication Type: Journal Article Peer Reviewed: Y **Publication Status:** 1-Published
Journal: AIP Advances
Publication Identifier Type: DOI Publication Identifier: 10.1063/1.5055887
Volume: 8 Issue: 11 First Page #: 115223
Date Submitted: 7/9/19 12:00AM Date Published: 11/1/18 12:00AM
Publication Location:
Article Title: Electrostatic tuning of mechanical and microwave resonances in 3D superconducting radio frequency cavities
Authors: Jacob M. Pate, Luis A. Martinez, Johnathon J. Thompson, Raymond Y. Chiao, Jay E. Sharping
Keywords: Cavity Quantum Electrodynamics
Abstract: We implement a non-contact, external method of simultaneously fine-tuning a mechanical resonator and a superconducting radio frequency (SRF) cavity using a capacitor formed between a silicon nitride membrane and a copper electrode at cryogenic temperatures. The silicon nitride membrane forms a variable boundary condition for the SRF cavity thereby creating the optomechanical cavity. By controlling the DC voltage applied between an external electrode and the silicon nitride membrane we are capable of tuning the resonance frequency internal to the SRF cavity up to 25 kHz for a cavity with loaded quality factor of 2.5 million, corresponding to six cavity linewidths. At the same time we observe the electrostatic frequency shift of the membrane. This approach has the unique benefit of avoiding any dielectric insertion or added gaps due to a moving end-wall thereby limiting the loss of the cavity.
Distribution Statement: 1-Approved for public release; distribution is unlimited.
Acknowledged Federal Support: **Y**

Publication Type: Journal Article Peer Reviewed: Y **Publication Status:** 1-Published
Journal: New Journal of Physics
Publication Identifier Type: DOI Publication Identifier: 10.1088/1367-2630/18/11/113015
Volume: 18 Issue: 11 First Page #: 113015
Date Submitted: 7/9/19 12:00AM Date Published: 11/1/16 12:00AM
Publication Location:
Article Title: Electromagnetic coupling to centimeter-scale mechanical membrane resonators via RF cylindrical cavities
Authors: Luis A Martinez, Alessandro R Castelli, William Delmas, Jay E Sharping, Raymond Chiao
Keywords: Resonators, coupling
Abstract: We present experimental and theoretical results for the excitation of a mechanical oscillator via radiation pressure with a room-temperature system employing a relatively low-(Q) centimeter-size mechanical oscillator coupled to a relatively low-Q standard three-dimensional radio-frequency (RF) cavity resonator. We describe the forces giving rise to optomechanical coupling using the Maxwell stress tensor and show that nanometer-scale displacements are possible and experimentally observable. The experimental system is composed of a 35 mm diameter silicon nitride membrane sputtered with a 300 nm gold conducting film and attached to the end of a RF copper cylindrical cavity.
Distribution Statement: 1-Approved for public release; distribution is unlimited.
Acknowledged Federal Support: **Y**

Publication Type: Journal Article Peer Reviewed: Y **Publication Status:** 1-Published
Journal: Fortschritte der Physik
Publication Identifier Type: DOI Publication Identifier: 10.1002/prop.201600066
Volume: 65 Issue: First Page #: 1600066
Date Submitted: 7/9/19 12:00AM Date Published: 6/1/17 12:00AM
Publication Location:
Article Title: Interaction of gravitational waves with superconductors
Authors: N. A. Inan, J. J. Thompson, R. Y. Chiao
Keywords: Gravitational waves
Abstract: Applying the Helmholtz Decomposition theorem to linearized General Relativity leads to a gauge-invariant formulation wherethe transverse-traceless part of the metric perturbation describes gravitational waves in matter. Gravitational waves incident on a superconductor can be described by a linear London-like constituent equation characterized by a “gravitational shear modulus” and a corresponding plasma frequency and penetration depth. Electric-like and magnetic-like gravitational tensor fields are defined in terms of the strain field of a gravitational wave. It is shown that in the DC limit, the magnetic-like tensor field is expelled from the superconductor in a gravitational Meissner-like effect.
Distribution Statement: 1-Approved for public release; distribution is unlimited.
Acknowledged Federal Support: **Y**

COVER SHEET

DARPA-BAA-14-46

UNIVERSITY OF CALIFORNIA, MERCED

PROFESSOR JAY SHARPING

(1) Report date	2/21/2019
(2) Report type	Final report
(3) Dates covered	9/1/2015-3/30/2019
(4) Title	Generation and frequency conversion of quantum states in high "Q" SRF parametric oscillators
(5) Contract number	W911NF1510557
(6) Authors	Jay E Sharping
(7) Performing organization	The Regents of the University of California Natural Sciences UNIVERSITY OF CALIFORNIA, MERCED 5200 NORTH LAKE ROAD MERCED CA 95343-5705
(8) Sponsoring organization	DARPA DSO administered by ARO

Generation and frequency conversion of quantum states in high “Q” SRF parametric oscillators

Abstract

We aim to experimentally study squeezing in a new type of opto-mechanical parametric oscillator. Our scheme is unique because it employs an effective nonlinearity arising from the quadratic response in the displacement of a membrane to the magnetic field present at the membrane’s surface. The potential impacts of this and our related projects in this area are that the proposed systems provide experimental connections between quantum, classical and relativistic physical domains through a phenomenon called the dynamical Casimir effect (DCE). In this program we focus on squeezing associated with the parametric generation of correlated pairs of real photons from electromagnetic quantum vacuum fluctuations. As such, these devices can generate entangled photons and can be broadly used for quantum information processing. The tasks in Phase 1 of this program fall into two thrusts: 1) we will investigate a high-Q superconducting radio-frequency parametric oscillator operating just below threshold to generate squeezed states at microwave frequencies of 11 GHz; and 2) we will theoretically explore the use of parametric frequency conversion to convert from microwave to optical frequencies. **We have made considerable progress in demonstrating opto-mechanical effects in our cavities but have not yet achieved sufficiently high Q-factors to observe above-threshold DCE or squeezing. The project effort shifted into two threads: 1) testing new cavity designs alternatives with which we could observe higher Q-factors; and 2) testing new cavity designs alternatives with which we could observe higher optomechanical coupling.**

Section I Summary of workplan and tasks

Phase I is an 18-month effort with a budget of $200,000 to evaluate the expected performance of such a scheme and to demonstrate squeezing of RF fields.

The key tasks are:

1) Quantify the oscillation threshold for a degenerate parametric oscillator in terms of cavity Q, and frequency of operation.
2) Quantify the fundamental and practical limits to squeezing in such a device.
3) Determine the merits and drawbacks of quadrature squeezing in a degenerate scheme vs. two-mode squeezing in a nondegenerate scheme.
4) Implement an experimental apparatus for squeezing generation at microwave frequencies.
5) Implement an experimental apparatus for squeezing measurements at microwave frequencies.

6) Quantify the fundamental and practical limits associated with the fidelity of transferring the squeezed state from microwave to optical frequencies.

The 6 tasks listed above fall into 3 categories: 1) SRF cavity design, fabrication and test (we will build one prototype and then a second SRF cavity); 2) measurement apparatus design, implementation and test; and 3) theoretical support.

Phase II is an additional 18-month effort with a budget of $200,000 to demonstrate the frequency conversion of squeezed RF fields to optical frequencies. The key tasks are:

1) Implement optical input/output access to the dilution refrigerator and implement an optical channel for Doppler shifting of the optical field in the presence of the moving SRF cavity membrane.
2) Implement and test the optical squeezing characterization circuit.
3) Quantify the efficiency of squeezing translation in such a device.

Section II Summary of Accomplishments

II-A Normal mode splitting in coupled SRF cavities

Three-dimensional radio frequency cavities demonstrate excellent frequency selectivity and, as such, are known for their use in RF filters. These cavities have potential applications in quantum information science, precision displacement metrology, and quantum electrodynamics. Additionally, coupled cavities that form a spectral doublet allow for parametric gain when incorporating mechanical elements. Here, we investigate normal-mode splitting in a pair of quarter-wave stub microwave cavities at room temperature and cryogenic environments in order to identify coupling mechanics for normal and superconducting systems. Superconducting quarter-wave stub cavities with a resonant frequency of 10 GHz are made from reactor-grade niobium and exhibit Q ranging from 10^5 to 10^9. We varied coupling from the weak coupling regime to the strong coupling regime. The minimum observed doublet separation was 7 MHz for room temperature tests and 200 kHz for cryogenic tests. We also report on values of intrinsic quality factor for the tuning cavity as a dielectric rod is translated along its symmetry axis. The realization of coupled superconducting radio-frequency cavities of this type is a necessary step towards implementation of parametric SRF-mechanical gain.

See full paper in the appendix.

II-B Electrostatic tuning of SRF cavities

We implement a non-contact, external method of simultaneously fine-tuning a mechanical resonator and a superconducting radio frequency (SRF) cavity using a capacitor formed between a silicon nitride membrane and a copper electrode at cryogenic temperatures. The silicon nitride membrane forms a variable boundary condition for the SRF cavity thereby creating the optomechanical cavity. By controlling the DC voltage applied between an external electrode and the silicon nitride membrane we are capable of tuning the resonance frequency internal to the SRF cavity up to 25 kHz for a cavity with loaded quality factor of 2.5 million, corresponding to six cavity linewidths. At the same time we observe the electrostatic frequency shift of the membrane. This approach has the unique benefit of avoiding any dielectric insertion or added gaps due to a moving end-wall thereby limiting the loss of the cavity. Furthermore, this design avoids applied pressure typically used with piezoelectric devices in accelerator cavities. This work seeks to have strong impact in tuning high-Q cavities due to its ability to maintain low losses.

See full paper in the appendix.

II-C Electromagnetic coupling to centimeter-scale mechanical membrane resonators via RF cylindrical cavities

We present experimental and theoretical results for the excitation of a mechanical oscillator via radiation pressure with a room-temperature system employing a relatively low-(Q) centimeter-size mechanical oscillator coupled to a relatively low-Q standard three-dimensional radio-frequency (RF) cavity resonator. We describe the forces giving rise to optomechanical coupling using the Maxwell stress tensor and show that nanometer-scale displacements are possible and experimentally observable. The experimental system is composed of a 35mmdiameter silicon nitride membrane sputtered with a 300 nm gold conducting film and attached to the end of a RF copper cylindrical cavity. The RF cavity is operated in its TE011mode and amplitude modulated on resonance with the fundamental drum modes of the membrane. Membrane motion is monitored using an unbalanced, non-zero optical path difference, optically filtered Michelson interferometer capable of measuring sub-nanometer displacements.

See full paper in the appendix.

II-D Simulation analysis of practical cavity designs

In this paper we report on designs, simulations and experiments with two types of high-Q 3-dimensional cavities: cylindrical TE011, and coaxial quarter-wave stub. We investigate the dependence of Q on the practical implementation tolerances of gaps between components, shape imperfections, and frequency tuning strategies. We find that cylindrical cavities can maintain high Q for designs which include frequency tunability and mechanical oscillators as long as extraordinary care is taken with shape and gap tolerance during construction and assembly. Coaxial stub cavities can be made frequency tunable while maintaining high Q, but require more creativity to include a mechanical element. Finally, we report on a coaxial stub cavity incorporating a conically-shaped stub which confines the electric field near the stub's tip stub, thus enhancing field-matter interactions near the tip.

See full paper in the appendix.

II-E A parametric oscillator for classroom demonstration or student laboratory

We describe a simple and intuitive parametric oscillator apparatus which is suitable for a classroom demonstration or an upper division laboratory. In order to facilitate the incorporation of this apparatus into the physics curriculum, we provide the learning objectives for an upper-division physics laboratory experiment. We present typical experimental data illustrating the main features of parametric oscillators including oscillation threshold, frequency shifting at large amplitude and bistability. Our experiments and theory emphasize identifying the lowest-order threshold for oscillation in terms of the modulation depth and quality factor. This experiment provides a foundation for understanding current research such as that in quantum opto-mechanics and nonlinear dynamics.

See full paper in the appendix.

II-E Executive summary slide

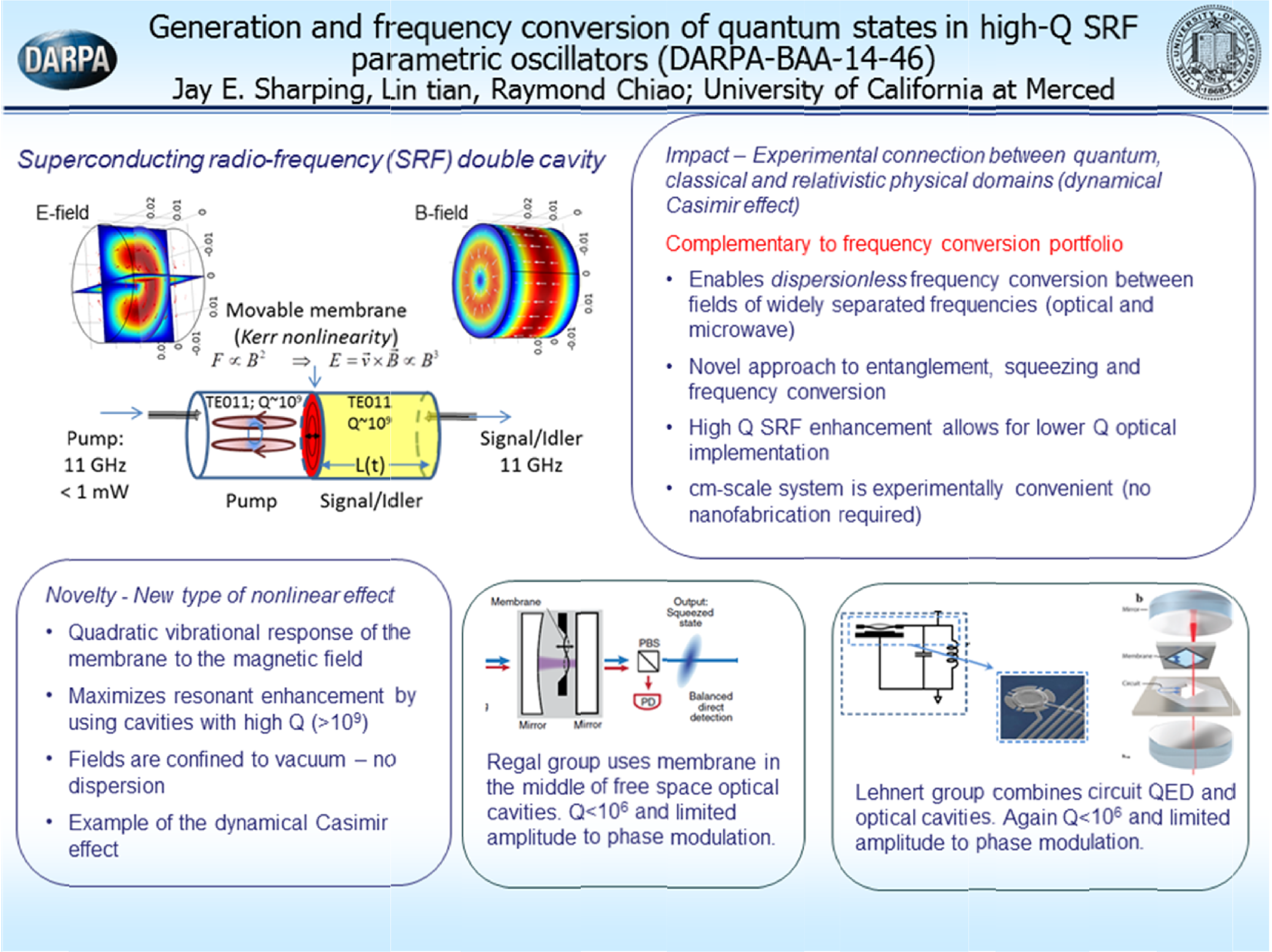

Generation and frequency conversion of quantum states in high-Q SRF parametric oscillators (DARPA-BAA-14-46)

Jay E. Sharping, Lin tian, Raymond Chiao; University of California at Merced

Superconducting radio-frequency (SRF) double cavity

Impact – Experimental connection between quantum, classical and relativistic physical domains (dynamical Casimir effect)

Complementary to frequency conversion portfolio

- Enables *dispersionless* frequency conversion between fields of widely separated frequencies (optical and microwave)
- Novel approach to entanglement, squeezing and frequency conversion
- High Q SRF enhancement allows for lower Q optical implementation
- cm-scale system is experimentally convenient (no nanofabrication required)

Novelty - New type of nonlinear effect

- Quadratic vibrational response of the membrane to the magnetic field
- Maximizes resonant enhancement by using cavities with high Q ($>10^9$)
- Fields are confined to vacuum – no dispersion
- Example of the dynamical Casimir effect

Regal group uses membrane in the middle of free space optical cavities. $Q<10^6$ and limited amplitude to phase modulation.

Lehnert group combines circuit QED and optical cavities. Again $Q<10^6$ and limited amplitude to phase modulation.

Section III Detailed Proposal Information

III-A Statement of Work

The workplan and task descriptions describe in detail each of the major tasks which are part of Phase I of this proposal.

	Start	End	% Compl.
Workplan	9/1/15	2/28/17	0%
Quantify expected performance of degenerate parametric oscillator	9/1/15	10/6/15	0%
Refine oscillation threshold calculation	9/1/15	10/6/15	0%
Refine output power calculation	9/1/15	10/6/15	0%
Fundamental and practical limits to squeezing study	1/1/16	10/25/16	0%
Theoretical model of squeezing in the SRF cavity oscillator	1/1/16	5/20/16	0%
Incorporate limitations of measurment apparatus to model	5/20/16	7/12/16	0%
Explore system design choices for best squeezing	7/12/16	10/25/16	0%
Degenerate vs two-mode squeezing	5/20/16	9/2/16	0%
Theoretical model of two-mode squeezing	5/20/16	7/12/16	0%
Identify practical issues (filtering/LO) for 2-mode squeezing	7/12/16	9/2/16	0%
Implement SRF oscillator for squeezing	9/1/15	10/8/16	0%
Detailed design of degenerate system	9/1/15	11/10/15	0%
System build including materials acquisition	11/10/15	2/5/16	0%
Dilution refrigerator feedtrhough modifications	9/1/15	12/15/15	0%
System test	2/5/16	5/21/16	0%
System enhancement/rebuild	5/21/16	6/7/16	0%
System #2 build	6/7/16	7/30/16	0%
System #2 test	7/30/16	10/8/16	0%
Implement squeezing measurement apparatus	11/10/15	2/26/17	0%
Design mixer/heterodyne measurement apparatus	11/10/15	1/1/16	0%
Acquire classical amplifiers, filters, other system components	1/1/16	2/23/16	0%
Room temperature measurements with detector	2/23/16	4/16/16	0%
Calibrate amplifiers using resistors at several temperatures	4/16/16	6/7/16	0%
Test phase preserving linear degenerate amplifier performance	10/8/16	11/30/16	0%
Characterize squeezing in degenerate sub-threshold oscillator	10/8/16	2/26/17	0%
Fundamental and practical limits to frequency translation fidelity	9/2/16	2/28/17	0%
Develop model for frequency translation fidelity	9/2/16	1/7/17	0%
Parametric study of translation fidelity issues	1/7/17	2/28/17	0%

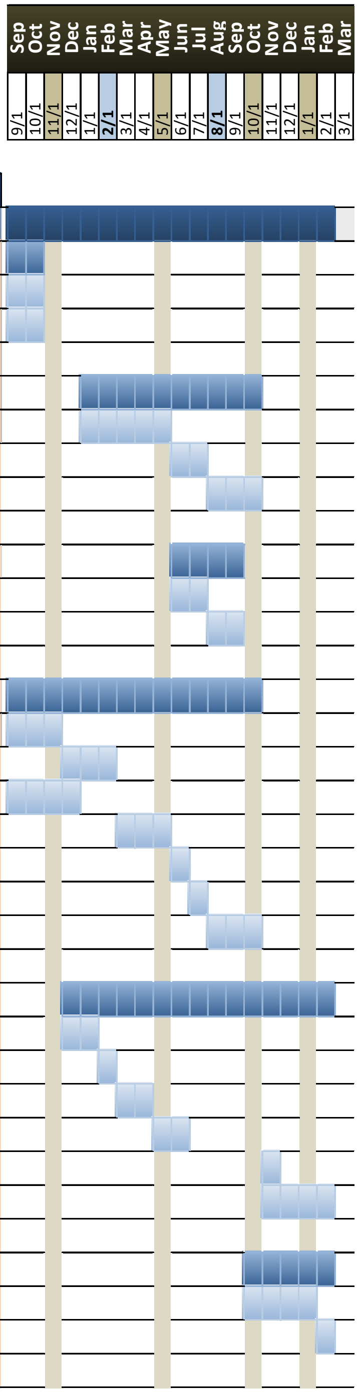

Workplan task	Benchmark	Goal	Description
Quantify expected performance of degenerate parametric oscillator			
Refine oscillation threshold calculation	Input power	<300 μW	Relationship for nondegenerate parametric device is inversely proportional to Q^3, but the nondegenerate case has not been verified from as many perspectives. Degeneracy factors may also introduce coefficients which may increase or decrease the threshold by a factor of 2.
Refine output power calculation	Output power	>50 nW	We have estimated the output power of an oscillator above threshold, but the power of the oscillator below threshold, where this experiment is conducted, is not known. Values on the order of nW are necessary in order to measure output fields using without the aid of phase-preserving preamplifiers.
Fundamental and practical limits to squeezing study			
Theoretical model of squeezing in the SRF cavity oscillator	Parameters estimated	Report	At present, our estimations of squeezing are based on extrapolations from related literature. In this task we start from first principles and attempt to model our system in order to obtain better estimates of anticipated results and to identify potential problems early in the project.
Incorporate limitations of measurment apparatus to model	Parameters estimated	Report	In this task we add measurement apparatus performance such as added noise and gain so that we can estimate the measurement results. In this effort we also investigate the detector calibration approach.
Explore system design choices for best squeezing	Parameters estimated	Report	In this task we provide a list of recommendations for the second iteration of the system which is informed by these theoretical exercises.
Degenerate vs two-mode squeezing			
Theoretical model of two-mode squeezing	Squeezing comparison	Report	In a related project, we are building a nondegenerate parametric oscillator. It may be the case that using nondegnerate signal and idler will produce two-mode squeezing that is easier to evaluate, or that produces more squeezing. The goal of this task is to quantify the value in trying to observe squeezing in the other system.
Identify practical issues (filtering/LO) for 2-mode squeezing	System conceptual design	Report	From a practical perspective it will be necessary to make distinguishible measurements of each mode in the 2-mode system. This would require filtering schemes which are not necessary in the degenerate case. In this task we identify the additional components needed for the detector in order to conduct the two-mode experiment if we choose to do that.

Workplan task	Benchmark	Goal	Description
Implement SRF oscillator for squeezing			
Detailed design of degenerate system	Detailed design	Specification	Here we create solid works diagrams and a requirements document for the SRF cavity system. This document should be of sufficient detail that a contract machinist can complete the build of the device without significant further input.
System build including materials acquisition	Hardware	SRF double cavity system	In this task we acquire raw materials, subcomponents such as the Nb coated membrane, and buid or have the system machined to specifications. The deliverable here is a physical cavity ready for test in the dilution refrigerators. Additional time is included for materials acquisition as high purity Nb often has 1-2 month lead time for delivery
Dilution refrigerator feedtrhough modifications	Hardware	Feedthrough modifications done	In this task we make any needed changes to the SMA feedthroughs in the dilution refrigerator. Past experience indicates that minor modifications are almost always necessary in order to include circulators, attenuators, isolators and amplifiers. In this case, inclusion of the calibration resistors is important.
System test	High Q and degenerate parametric oscillation	$Q>10^9$ Oscillation above threshold	Here we perform several iterations (probably 6) of cooling and test in order to evaluate the degenerate oscillator system. We are not looking for squeezing. Rather we are testing cavity frequency control (under construction in a related project), pumping, and detection of output signals. A critical exercise is establishing critical (or under) coupling of the pump and pickup loop antennas.
System enhancement/rebuild	Detailed design	Specification	The project has two iterations of system build where the first is a prototype. We anticipate the need to build a second cavity because certain issues are likely to reveal themselves only after system test. One example is the relative value of side vs end coupling.
System #2 build	Hardware	SRF double cavity system	In this task we carry out the second iteration of cavity build or have the system machined to specifications. The deliverable here is a physical cavity ready for test in the dilution refrigerators.
System #2 test	High Q and degenerate parametric oscillation	$Q>10^9$ Oscillation above threshold	Here we perform several iterations (probably 6) of cooling and test in order to evaluate the degenerate oscillator system. We will look for squeezing in this iteration as we should have the calibrated detection circuit available.
Implement squeezing measurement apparatus			
Design mixer/heterodyne measurement apparatus	Detailed design	Full parts specification	In this task we design the detection circuit including all amplifiers, attenuators, circulators, resistors (for calibration) and mixers. The scheme is similar to that used by many researchers working in the circuit QED field. Since we have not done this before we need to carefully design the system and identify the parts needed. We do, however, already have HEMT amplifiers and a variety of RF components for rapid prototyping.
Acquire classical amplifiers, filters, other system components	Parts list	Parts on hand	Here we acquire any additional parts as specified in the above task. This is listed separately because some compoents have 1-2 month lead times.
Room temperature measurements with detector	Complete detection system	Operational detection circuit	The goal of this task is to assemble the complete detection system with the exception of the low temperature components. Testing using weak input signals is performed.
Calibrate amplifiers using resistors at several temperatures	Gain and relative noise	Sufficient to extract squeezing in SRF cavity	The goal of this task is to calibrate the detection system by using resistors in the dilution refrigerator. A critical reason for this as a separate task is that dilution refrigerator feed throughs are difficult to access and temperature cycling sometimes causes connection problems. It is critical to do subsystem testing with short circuits through the dilution refrigerator.
Test phase preserving linear degenerate amplifier performance	Gain and phase-sensitive performace	Operating as a phase preserving amplifier	The goal of this task is to evaluate the phase-preserving gain of the cavity parametric device. Here we inject a weak signal into the side opposite the pump and characterize the gain. This is not a squeezing exercise.
Characterize squeezing in degenerate sub-threshold oscillator	Squeezing	A convincingly quantum mechanical signal	Here we arrive at the main goal of our study. We will observe the sub-threshold squeezed output emerging from the signal/idler portion of the SRF cavity.

Workplan task	Benchmark	Goal	Description
Fundamental and practical limits to frequency translation fidelity			
Develop model for frequency translation fidelity	Parameters estimated	Report	This theoretical exercise give a basis for using the proposed system as a resource for squeezing and subsequently translating the mode to optical frequencies. Initially we will consider a free-space optical beam incident on the membrane which is Doppler shifted. Then we will consider other possibilities such as including an optical cavity.
Parametric study of translation fidelity issues	Parameters estimated	Report	In this task we obtain a high level design for the frequency translation scheme

Phase II workplan

	Start	End	% Compl.
Workplan	3/1/17	8/27/18	0%
Implement optical Doppler shifting from the moving cavity membrane	3/1/17	11/2/17	0%
Implement optical access to Dilution refrigerator incuding cavity	3/1/17	7/2/17	0%
Implement Doppler shifting measurement	7/2/17	11/2/17	0%
Implement and test the optical squeezing characterization circuit.	6/1/17	12/23/17	0%
Assemble balanced squeezing detection system	6/1/17	8/22/17	0%
Characterize detection system using SNL light source	8/22/17	10/22/17	0%
Attempt to observe signal deflected from membrane	10/22/17	12/23/17	0%
Quantify the efficiency of squeezing translation in such a device.	12/23/17	8/27/18	0%
First squeezing measurements and debugging	12/23/17	3/15/18	0%
Squeezing as a function of RF power	3/15/18	6/5/18	0%
Squeezing as a function of optical power	6/5/18	8/27/18	0%

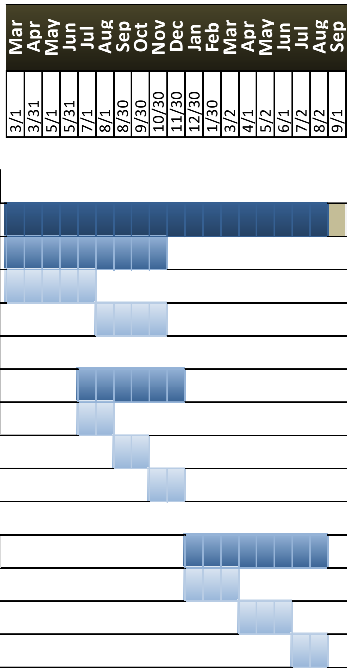

References

1. T. P. Purdy, P. -. Yu, R. W. Peterson, N. S. Kampel, and C. A. Regal, "Strong Optomechanical Squeezing of Light," Physical Review X **3,** 031012 (2013).

2. H. B. G. Casimir, "On the attraction between two perfectly conducting plates," Proceedings Koninklijke Akademie van Wetenschappen te Amsterdam **51,** 793-796 (1948).

3. V. V. Dodonov and A. V. Dodonov, "Quantum harmonic oscillator and nonstationary Casimir effect," Journal of Russian Laser Research **26,** 2664-2682 (2005).

4. P. D. Nation, J. R. Johansson, M. P. Blencowe, and F. Nori, "Colloquium: Stimulating uncertainty: Amplifying the quantum vacuum with superconducting circuits," Reviews of Modern Physics **84,** 1-24 (2012).

5. C. M. Wilson, G. Johansson, A. Pourkabirian, M. Simoen, J. R. Johansson, T. Duty, F. Nori, and P. Delsing, "Observation of the dynamical Casimir effect in a superconducting circuit," Nature **479,** 376-379 (2011).

6. L. P., P. G.S., H. J., and H. P.J., "Dynamical Casimir effect in a Josephson metamaterial," Proceedings of the National Academy of Science **110,** 4234-4238 (2013).

7. L. Tian, "Optoelectromechanical transducer: Reversible conversion between microwave and optical photons," Annalen der Physik **527,** 1-14 (2015).

8. R. W. Andrews, R. W. Peterson, T. P. Purdy, K. Cicak, R. W. Simmonds, C. A. Regal, and K. W. Lehnert, "Bidirectional and efficient conversion between microwave and optical light," Nature Physics **10,** 321-326 (2014).

9. T. A. Palomaki, J. W. Harlow, J. D. Teufel, R. W. Simmonds, and K. W. Lehnert, "Coherent state transfer between itinerant microwave fields and a mechanical oscillator," Nature **495,** 210-214 (2013).

10. A. H. Safavi-Naeini, S. Groeblacher, J. T. Hill, J. Chan, M. Aspelmeyer, and O. Painter, "Squeezed light from a silicon micromechanical resonator," Nature **500,** 185-189 (2013).

11. K. Qu and G. S. Agarwal, "Strong squeezing via phonon mediated spontaneous generation of photon pairs," New Journal of Physics **16,** 113004 (2014).

12. S. Chaturvedi, K. Dechoum, and P. D. Drummond, "Limits to squeezing in the degenerate optical parametric oscillator," Physical Review a **65,** 033805 (2002).

13. T. Eberle, S. Steinlechner, J. Bauchrowitz, V. Haendchen, H. Vahlbruch, M. Mehmet, H. Mueller-Ebhardt, and R. Schnabel, "Quantum Enhancement of the Zero-Area Sagnac

Interferometer Topology for Gravitational Wave Detection," Phys. Rev. Lett. **104,** 251102 (2010).

14. Y. Takeno, M. Yukawa, H. Yonezawa, and A. Furusawa, "Observation of-9 dB quadrature squeezing with improvement of phase stability in homodyne measurement," Optics Express **15,** 4321-4327 (2007).

15. M. A. Castellanos-Beltran, K. D. Irwin, G. C. Hilton, L. R. Vale, and K. W. Lehnert, "Amplification and squeezing of quantum noise with a tunable Josephson metamaterial," Nature Physics **4,** 929-931 (2008).

16. M. Abdi and A. R. Bahrampour, "Effect of higher-order waves in parametric oscillatory instability in optical cavities," Phys. Scripta **83,** 045401 (2011).

17. L. Tian, "Robust Photon Entanglement via Quantum Interference in Optomechanical Interfaces," Phys. Rev. Lett. **110,** 233602 (2013).

18. L. Tian, "Adiabatic State Conversion and Pulse Transmission in Optomechanical Systems," Phys. Rev. Lett. **108,** 153604 (2012).

19. P. Bernard, G. Gemme, R. Parodi, and E. Picasso, "A detector of small harmonic displacements based on two coupled microwave cavities," Rev. Sci. Instrum. **72,** 2428-2437 (2001).

20. C. E. Reece, P. J. Reiner, and A. C. Melissinos, "Parametric Converters for Detection of Small Harmonic Displacements," Nuclear Instruments & Methods in Physics Research Section A-Accelerators Spectrometers Detectors and Associated Equipment **245,** 299-315 (1986).

21. D. F. Walls and G. J. Milburn, *Quantum optics* (Springer, 2008).

22. R. Y. Chiao, L. A. Martinez, S. J. Minter, and A. Trubarov, "Parametric Oscillation of a Moving Mirror Driven by Radiation Pressure in a Superconducting Fabry-Perot Resonating System," ArXiv e-prints **eprint arXiv:1207.6885,** (2012).

23. R. Y. Chiao, R. W. Haun, N. A. Inan, B. -. Kang, L. A. Martinez, S. J. Minter, G. A. Munoz, and D. A. Singleton , "A Gravitational Aharonov-Bohm Effect, and Its Connection to Parametric Oscillators and Gravitational Radiation," in *Quantum Theory: A Two-Time Success Story.~ISBN 978-88-470-5216-1.~Springer-Verlag Italia, 2014, p.~213*, D. C. Struppa and J. M. Tollaksen , eds. 2014), pp. 213.

24. S. J. Minter, K. Wegter-McNelly, and R. Y. Chiao, "Do mirrors for gravitational waves exist?" Physica E-Low-Dimensional Systems & Nanostructures **42,** 234-255 (2010).

25. V. Braginsky, S. Strigin, and S. Vyatchanin, "Parametric oscillatory instability in Fabry-Perot interferometer," Phys. Lett. A **287,** 331-338 (2001).

26. T. Corbitt, D. Ottaway, E. Innerhofer, J. Pelc, and N. Mavalvala, "Measurement of radiation-pressure-induced optomechanical dynamics in a suspended Fabry-Perot cavity," Physical Review a **74,** 021802 (2006).

27. T. J. Kippenberg, H. Rokhsari, T. Carmon, A. Scherer, and K. J. Vahala, "Analysis of radiation-pressure induced mechanical oscillation of an optical microcavity," Phys. Rev. Lett. **95,** 033901 (2005).

Normal-mode splitting in coupled high-Q microwave cavities

A. R. Castelli, L. A. Martinez, J. M. Pate, R. Y. Chiao, and J. E. Sharping[1]

School of Natural Sciences, University of California at Merced, Merced,
California 95343, USA

(Dated: January 31, 2019)

Three-dimensional radio frequency cavities demonstrate excellent frequency selectivity and, as such, are known for their use in RF filters. These cavities have potential applications in quantum information science, precision displacement metrology, and quantum electrodynamics. Additionally, coupled cavities that form a spectral doublet allow for parametric gain when incorporating mechanical elements. Here, we investigate normal-mode splitting in a pair of quarter-wave stub microwave cavities at room temperature and cryogenic environments in order to identify coupling mechanics for normal and superconducting systems. Superconducting quarter-wave stub cavities with a resonant frequency of 10 GHz are made from reactor-grade niobium and exhibit Q ranging from 10^5 to 10^9. We varied coupling from the weak coupling regime to the strong coupling regime. The minimum observed doublet separation was 7 MHz for room temperature tests and 200 kHz for cryogenic tests. We also report on values of intrinsic quality factor for the tuning cavity as a dielectric rod is translated along its symmetry axis. The realization of coupled superconducting radio-frequency cavities of this type is a necessary step towards implementation of parametric SRF-mechanical gain.

PACS numbers: Valid PACS appear here

I. Introduction/Background

Three-dimensional superconducting radio frequency (SRF) cavities are commonly used in particle accelerators[1–5] because such high-quality factor (high-Q) cavities can efficiently sustain high electric-field strengths. These *low loss* cavities are gaining popularity as a platform for quantum electrodynamics (QED) as well. Many QED experiments involve the coupling of electromagnetic radiation to qubits[6]. For example, Reagor, et al., demonstrated the coupling to and readout of a transmon qubit coupled via a quarter-wave stub cavity[7]. Other important work involves coupling to mechanical elements which may behave classically or quantum-mechanically. Andrews, et al., demonstrate spectral and temporal mode conversion in a microwave circuit which includes a mechanical resonator[8], and Palomaki, et al., extend the concept to include coherent transfer of states between a microwave circuit and the mechanical oscillator[9]. Related work by Teufel et al., realizes *strong coupling* between the microwave and mechanical modes[10]. Noguchi, et al., perform experiments in which ground state cooling of a silicon nitride membrane inside an SRF cavity occurs[11]. A central theme in the work cited above is the integration of high-Q resonators (cavities or circuits)[12].

Normal-mode splitting occurs when two resonant subsystems, which are degenerate in frequency, are coupled with one another such that the rate of energy exchange is larger than the rate of energy loss[13]. Once obtained, normal-mode splitting gives one the ability to modify the coupled spectrum by modifying any combination of the resonances and the coupling strength. Motivated by the goal of constructing a dual cavity SRF parametric oscillator for QED, we present experimental results along with COMSOL simulations demonstrating normal-mode splitting in two high-Q SRF quarter-wave stub cavities coupled via a coaxial waveguide (Figure 1). This is the first investigation of normal-mode splitting in high-Q SRF coaxial stub cavities.

The locations of the peaks in the energy spectrum of the coupled cavity system are given by:

$$E_{\kappa\pm} = \frac{(E_L + E_R) \pm \sqrt{(E_L + E_R)^2 - 4\left(E_L E_R - \kappa^2\right)}}{2}, \tag{1}$$

where $E_{\kappa\pm}$ are the perturbed resonant peak energies of the system, $E_{L,R}$ refer to the unperturbed resonances of the cavities and κ is the cavity-to-cavity coupling. In order to obtain

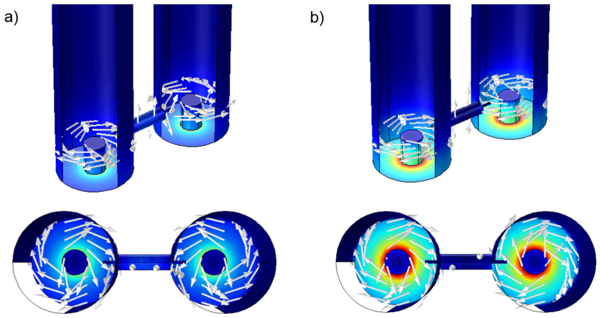

Figure 1. a) Symmetric and b) anti-symmetric modes of the magnetic field surface and volume densities for the dual stub cavity system modeled in COMSOL. Energy transfer occurs due to coupling between the two cavities facilitated by SMA cable.

the position of the spectral peaks as a function of the detuning of one cavity resonance frequency relative to the other we use $E_L = E_0$ and $E_R = E_0 + F$ in Eq. 1 where E_0 is the resonance of the fixed cavity and F represents the detuning of one cavity resonance relative to the other. For identical cavities degenerate in resonance frequency we set $E_L = E_R = E_0$ so that $E_{\kappa\pm} = E_0 \pm \kappa$ simplifies to obtain the minimum energy separation between the resonant peaks:

$$\Delta E_{min} = 2\kappa. \tag{2}$$

Note that it is apparent from Eq. 2 that the width of each resonance must be narrow relative to the coupling rate ($< 2\kappa$) which implies that the rate of energy loss for each cavity is small relative to the coupling of energy between them. This motivates our use of SRF cavities having large Q because by doing so we gain sensitivity to coupling mechanisms with small κ.

Since the quality factor for the SRF electromagnetic mode is such an important value we briefly describe how the intrinsic quality factor (Q_0), that which neglects the impact on overall Q due to input and output coupling, relates to the geometry of the cavity and the material used to construct it[14,15]. The presence of an electromagnetic field inside the cavity gives rise to currents which flow along the surface. Specifically, it is the supercurrents which arise from the expulsion of the magnetic field at the superconducting surface which limit the Q_0. In terms of energy, Q_0 represents the ratio of total energy stored in the cavity to power dissipated by surface and residual resistances. The expression for Q_0 is, therefore:

$$Q_0 = \frac{\omega_0 U_{tot}}{P_{diss}} = \frac{\omega_0 \mu_0 \iiint |\vec{H}|^2 dV}{R_S \iint |\vec{H}|^2 dS}, \tag{3}$$

in which ω_0 is the angular resonance frequency, U_{tot} is the total energy stored, P_{diss} is the dissipated power, $\vec{H}$ is the magnetic field and R_S is the surface resistance. Observe that the volume integral in the numerator accounts for the energy stored in the volume of the cavity, while the surface integral in the denominator accounts for the resistive losses within the London penetration depth on the inner surfaces of the cavity. Equation 3 captures the relationship between the resonant frequency, the shape of the resonant mode, and the superconducting qualities of the cavity walls. If we let the ratio of field energy volume density to field energy surface density equal a constant geometrical factor G, Q_0 now takes the form

$$Q_0 = \frac{G}{R_s} \tag{4}$$

where, for clarity,

$$G = \frac{\omega_0 \mu_0 \iiint |\vec{H}|^2 dV}{\iint |\vec{H}|^2 dS}, \tag{5}$$

is the geometrical factor that quantifies how well confined the mode is within the cavity.

II. Setup/Procedure

The basic configuration is shown in Figure 2 and the cavity design specifications are given in I. Normal-mode splitting experiments were performed both in room temperature and cryogenic environments. As such, the procedure for taking measurements must adjust to the limitations of measuring the experimental system at temperatures below 1 K. Specific methods are outlined for both environments in the following sections.

III. Room temperature experiments

These experiments utilized aluminum quarter-wave stub cavities whose cavity-to-cavity coupling κ is established by an approximately 13-mm long coaxial waveguide whose cladding was stripped at both ends thereby exposing the bare center conductor which was inserted

Table I. Cavity parameters

$f_0 = 10$ GHz	Resonance freq.
$L_{cyl} = 55$ mm	Cylinder height
$R_{cyl} = 7.0$ mm	Cylinder radius
$h_s = 5.0$ mm	Stub height
$r_s = 2.0$ mm	Stub radius

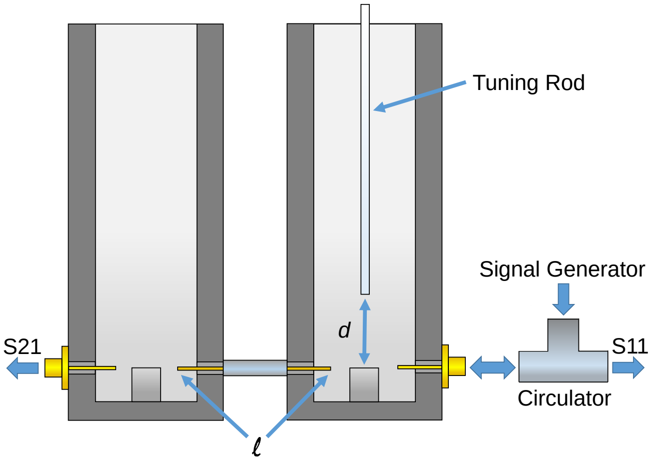

Figure 2. The double cavity system. Tuning of the right-hand cavity is performed through the variable insertion of a dielectric rod to obtain a variable gap, d. Input and output couplers are over-coupled while the insertion length, ℓ, of the coupling antennae is variable.

into the cavity through the cavity wall. The intrinsic quality factor of these cavities at room temperature is on the order of 10^3, so the wires must protrude into the cavity to achieve sufficient coupling. Measurements were taken using a network analyzer whose signal is coupled to the dual-cavity system via SMA cables connected to a coaxial connector mounted within each cavity's wall. These connectors were adjusted to near identical length and long enough to establish a large coupling from source to cavity. We tuned the frequency of the cavity using a dielectric rod connected to a translation stage which was oriented parallel to the cavity's symmetry axis. We then recorded the S21 transmission spectrum as a function of tuning rod position as the gap distance, d, between the stub and the end of the tuning rod increases. The corresponding cavity resonance frequency increases by roughly 300 MHz.

We control κ by adjusting the insertion length, ℓ, of the stripped coaxial center conductor into the cavity volume (Figure 2). The coupling antenna length varies from $\ell = 1.7$ mm (the under-coupled regime) to $\ell = 3.7$ mm (the over-coupled regime) in steps of 0.25 mm. As a result, we present plots of normal-mode splitting in the transmission spectra for coupled aluminum cavities for several values of κ.

Nine couplings were tested at room temperature and the cavity spectra for each run were mapped to 3D plots (Figure 3). Measurements were made as a function of the distance between the tip of the dielectric rod and the top of the cavity stub, d. The rod was centered such that it shared a symmetry axis with the cavity. We utilized very low power levels to keep the signal to noise ratio at acceptable levels.

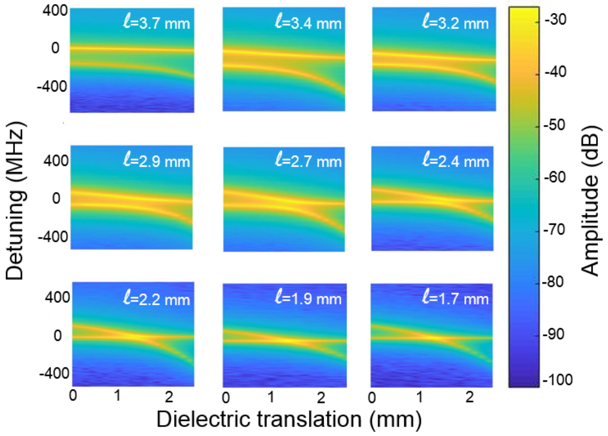

Figure 3. Experimental 3D plots of normal-mode splitting in an aluminum dual-cavity system at room temperature. The plots demonstrate coupling between cavities for antenna lengths ranging from $\ell = 3.7$ mm to $\ell = 1.7$ mm in steps of 0.25 mm. The measured κ increases as a function of increasing antenna length.

Each plot demonstrates the coupling strength between cavities through their spectral peak-to-peak separation in frequency space. Each cavity demonstrated a quality factor of approximately 10^3. For large κ (top left), the cavities "see" each other strongly and their resonances repel each other. As the antennae are removed from the cavity volumes (left to right), the electric and magnetic field interaction strength decreases until the cavities are effectively no longer coupled. We measured detunings of up to 400 MHz for all antenna lengths to ensure that we observed the full effect of the avoided crossing.

These spectra were further analyzed and the minimum peak-to-peak frequency separation of each doublet is plotted in Figure 4. The first data point corresponds to a normal frequency crossing while the others range in minimum peak separation from approximately 150 MHz to 7 MHz as the coupler antenna is translated out of each cavity volume. Unsurprisingly, we observed a downward trend for minimum peak separation as the antenna was removed. A plot of all these traces is shown in Figure 4.

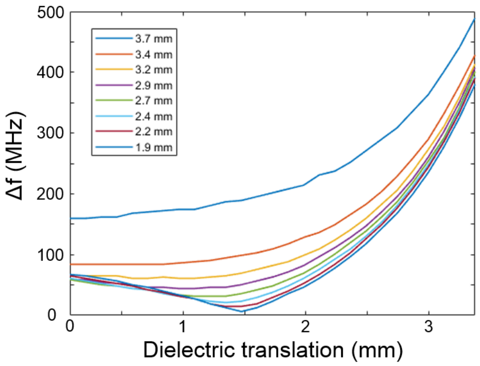

Figure 4. A composite of doublet peak frequency differences for room temperature experiments overlaid to demonstrate the downward trend in minimum peak separation as a function of cavity coupling.

A normal crossing for very small antenna size implied a limit to spectral doublet resolution for cavities operating at room temperature and therefore low Q.

IV. SRF experiments

Superconducting radio-frequency experiments were performed with niobium quarter-wave stub cavities in which κ was established through the use of a normally conducting 13-mm long coaxial waveguide similar to that used in the previously described room temperature experiments. The coupling antenna in these experiments does not protrude into the cavity, and thus the coupling is evanescent. The coupling coaxial waveguide length is as short as possible in order to avoid unwanted resonant modes in the coupling waveguide. For cavity tuning purposes, we utilize a sapphire rod mounted on a cryogenic linear drive (Janssen). A plot of stub cavity resonance versus calibrated drive translation distance is shown in Figure 5. Results indicate that the sapphire rod minimally perturbs the field after forming a gap of approximately 9 mm between the rod and the stub of the cavity.

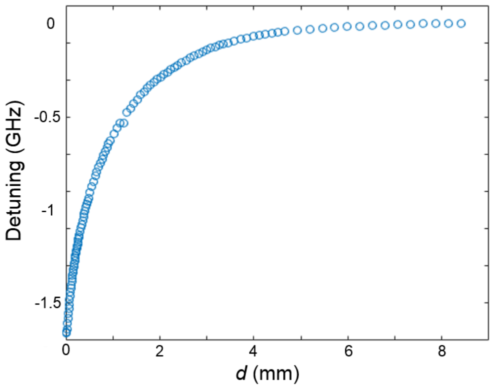

Figure 5. Calibrated tuning curve for a coaxial stub cavity resonance. The effective tuning range in this cavity is 1.7 GHz.

A signal generator fed a 10-GHz signal into the dilution refrigerator and subsequently into the dual-cavity system via an SMA cable. The length of the coupler for each cavity determined the signal-to-cavity coupling, C_{SRF}, for each cavity. A cryogenic circulator allows recording of both S11 and S21 signals. The S11 (reflected) signal feeds directly to a diode and then to a sourcemeter which measures the peak voltage. The S21 (transmitted) signal passes through a cryogenic HEMT amplifier at 4 K and another amplifier at room temperature before being detected by the diode and sourcemeter. The dual-cavity system is shown in greater detail in Figure 2. We recorded several spectra of both S11 and S21 while translating the dielectric rod through the point of dual-cavity degeneracy.

When the coupling antennae are recessed too far into the waveguide, $\ell = -1.3$ mm, κ is small and cannot be resolved under the cavity modes. Normal-mode splitting was not observed. Increasing κ by adjusting antenna length to $\ell = -0.8$ mm produced an observable splitting in both S11 and S21 measurements. Figure 6 shows the normal-mode splitting as well as a composite of measurements of S21 in the splitting region for a range of input powers.

Note that a measurable change in intrinsic quality factor occurs while tuning cavity as the tuning rod gap becomes small. While maintaining a critically coupled system at the point of interest in frequency space, we obtained several measurements of intrinsic Q as the rod was retracted from the cavity volume. These measurements are summarized in Table II.

Table II. Several values of Q_0 for different sapphire rod insertion distances. The values for β demonstrate how the input coupler length affects Q_0. A β of 55 implies extreme over-coupling and that Q_0 for this resonance is larger than indicated and most likely closer to the cavity's natural intrinsic Q of 2×10^8.

d (mm)	f_0 (GHz)	Q_0	β
7.0	10.5	2.8×10^7	55
2.1	10.236	1.1×10^6	0.96
0.8	9.8	8.4×10^5	0.47

The three sets of quantities shown in Table II represent the maximum, resonant and minimum of experimental measurement frequencies.

We performed measurements on a Nb dual-cavity system in dilution refrigerator under vacuum. Couplers were retracted into the coupling waveguide until they were recessed by approximately 1.5 mm behind the cavity wall. We took frequency spectra for reflection and transmission measurements much in the same way as we did for room temperature experiments. We first located the frequency doublet, placed the sapphire rod in the desired starting location by manually operating the drive, then recorded the spectra one at a time after moving the sapphire rod in increments of approximately 1 μm (lowest resolvable translation increment for the drive). Results from these measurements are displayed in Figures 6a) and 6b).

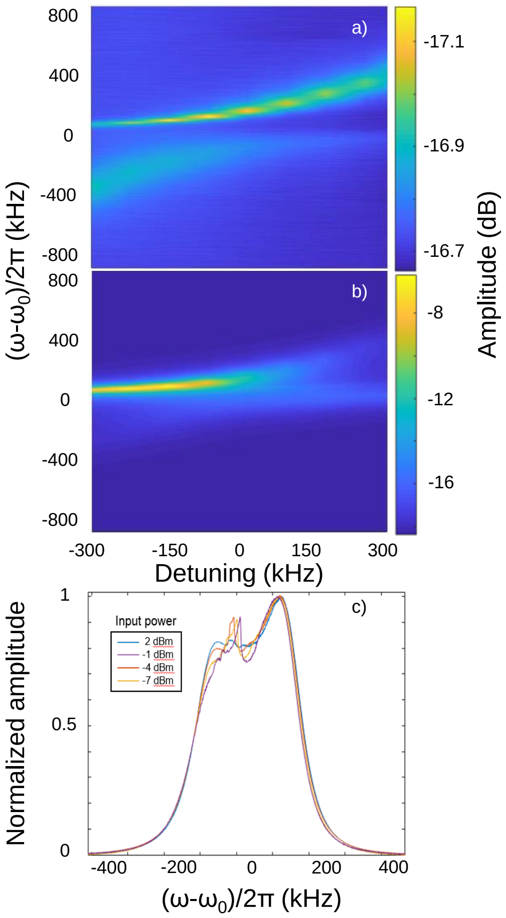

Figure 6. a) Experimental SRF S11 (reflection) signal for a cavity coupling corresponding to antenna length $\ell = -0.8$ mm. b) Experimental SRF S21 (transmission) signal for the same cavity coupling. c) Normalized experimental S21 signal spectra for a range of signal generator powers.

Additionally, we recorded several spectra for the avoided crossing transmission measurement as a function of input power to make sure we were not saturating either of the amplifiers used during these experiments. Input powers ranged from -7 to 2 dBm in increments of 3 dBm. The data for this test is shown in Figure 6c). As expected, the curves increase in amplitude for larger input powers, but the data has been normalized here so that any discrepancies between plots become immediately apparent. While the left peak demonstrates some strange behavior, the overall shape and position of the doublet does not appear to change.

Lastly, we plot the numerical values of the minimum peak separations for room temper-

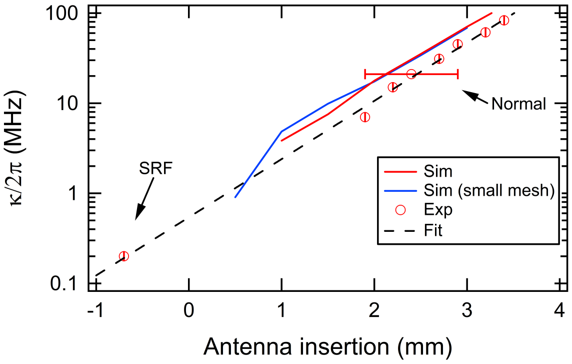

Figure 7. A semi-log plot of the minimum peak separation of the spectral doublet as a function of coupler antenna insertion for the SRF cavities and normal cavities. Symbols are experimental data and solid lines are simulations. The measurement uncertainty, illustrated by the error bar in the data, is dominated by uncertainty in the zero-point of antenna insertion. The dashed line is drawn to show the consistency between the normal and SRF cavities.

ature and SRF measurements in Figure 7. Positive values to room temperature (normal) tests as these experiments required strong coupling directly to the fields of the cavity. The value at $\ell = -0.8\ mm$ corresponds to the single SRF measurement. As mentioned previously, coupling efficiently to our high-Q stub cavities requires a recessed center pin for evanescent coupling which does not perturb the cavity mode and degrade the Q. The SRF case yielded a minimum peak-to-peak frequency separation of approximately 200 kHz which is an order of magnitude smaller than the minimum separation for the smallest κ case from room temperature experiments. Considering the cavity Q is four orders of magnitude higher in cryogenic environment, one can infer that it would be difficult to raise the Q high enough to observe an even smaller minimum separation. When considering the implementation of this system into an optomechanical design, a separation of 10-100 kHz seems ideal for incorporating small mechanical components.

V. Conclusions

In summary, we have demonstrated a tunable SRF cavity with a resonance that can be tuned by as much as 1.7 GHz with an average frequency of 10 GHz. This tuning is possible while maintaining a $Q \sim 10^6$. We coupled the tunable cavity to a second fixed-frequency SRF cavity in order to observe normal-mode splitting with a minimum coupling of 200 kHz.

We used a sapphire rod for frequency tuning which results in a reduction of Q along with the cavity frequency. We expect that constructing a coaxial stub cavity with an axial hole will allow for frequency tuning which has less impact on Q. If the cavity Q remains $> 10^8$ while tuning, then couplings as small as 100 Hz will be resolvable.

Our system is potentially useful for optomechanical experiments[16] because one can produce a coupling rate which will enhance a wide range of mechanical resonance frequencies. It is a platform for cQED experiments such as Raman scattering[17] and optomechanically-induced transparency[16,18]. Ultra-sensitive optomechanical sensors may ultimately be useful as detectors of gravatational waves[19–22]. Recently, superconducting coaxial RF cavities and microwave circuits have been garnering attention in the field of quantum computing as well[23,24]. These cavities can also be used as an RF filter for a variety of applications such as acting as the low-pass filter in an optoelectronic oscillator[25,26].

References

[1] A. Romanenko, F. Barkov, L. Cooley, and A. Grassellino, "Proximity breakdown of hydrides in superconducting niobium cavities," Superconductor Science and Technology **26**, 035003 (2013).

[2] A. Grassellino, A. Romanenko, D. Sergatskov, O. Melnychuk, Y. Trenikhina, A. Crawford, A. Rowe, M. Wong, T. Khabiboulline, and F. Barkov, "Nitrogen and argon doping of niobium for superconducting radio frequency cavities: a pathway to highly efficient accelerating structures," Superconductor Science and Technology **26**, 102001 (2013).

[3] R. E. Ricker and G. R. Myneni, "Evaluation of the propensity of niobium to absorb hydrogen during fabrication of superconducting radio frequency cavities for particle accelerators," Journal of research of the National Institute of Standards and Technology **115**, 353 (2010).

[4] G. Ciovati, "Effect of low-temperature baking on the radio-frequency properties of niobium superconducting cavities for particle accelerators," Journal of Applied Physics **96**, 1591–1600 (2004).

[5] H. Padamsee, K. Jens, and H. Tom, "Rf superconductivity for accelerators," New York.

A Wiely-Interscience Publication , 129–144 (1998).

[6] H. Paik, D. Schuster, L. S. Bishop, G. Kirchmair, G. Catelani, A. Sears, B. Johnson, M. Reagor, L. Frunzio, L. Glazman, *et al.*, "Observation of high coherence in josephson junction qubits measured in a three-dimensional circuit qed architecture," Physical Review Letters **107**, 240501 (2011).

[7] M. Reagor, W. Pfaff, C. Axline, R. W. Heeres, N. Ofek, K. Sliwa, E. Holland, C. Wang, J. Blumoff, K. Chou, M. J. Hatridge, L. Frunzio, M. H. Devoret, L. Jiang, and R. J. Schoelkopf, "Quantum memory with millisecond coherence in circuit qed," Phys. Rev. B **94**, 014506 (2016).

[8] R. Andrews, A. Reed, K. Cicak, J. Teufel, and K. Lehnert, "Quantum-enabled temporal and spectral mode conversion of microwave signals," Nature communications **6**, 10021 (2015).

[9] T. Palomaki, J. Harlow, J. Teufel, R. Simmonds, and K. Lehnert, "Coherent state transfer between itinerant microwave fields and a mechanical oscillator," Nature **495**, 210 (2013).

[10] J. Teufel, D. Li, M. Allman, K. Cicak, A. Sirois, J. Whittaker, and R. Simmonds, "Circuit cavity electromechanics in the strong-coupling regime," Nature **471**, 204 (2011).

[11] A. Noguchi, R. Yamazaki, M. Ataka, H. Fujita, Y. Tabuchi, T. Ishikawa, K. Usami, and Y. Nakamura, "Ground state cooling of a quantum electromechanical system with a silicon nitride membrane in a 3d loop-gap cavity," New Journal of Physics **18**, 103036 (2016).

[12] M. Reagor, H. Paik, G. Catelani, L. Sun, C. Axline, E. Holland, I. M. Pop, N. A. Masluk, T. Brecht, L. Frunzio, *et al.*, "Reaching 10 ms single photon lifetimes for superconducting aluminum cavities," Applied Physics Letters **102**, 192604 (2013).

[13] P. Von Brentano and M. Philipp, "Crossing and anticrossing of energies and widths for unbound levels," Physics Letters B **454**, 171–175 (1999).

[14] G. Ciovati, "Review of the frontier workshop and q-slope results," Physica C-Superconductivity and its Applications **441**, 1 (2006), pT: J; CT: 12th International Workshop on RF Superconductivity; CY: JUL 10-15, 2005; CL: Cornell Univ, Ithaca, NY; TC: 8; UT: WOS:000238875600009.

[15] C. E. Reece and G. Ciovati, "Superconducting radio-frequency technology rd for future accelerator applications," Reviews of Accelerator Science and Technology, Vol 5: Applications of Superconducting Technology to Accelerators , 285–312 (2012), pT: S; UT: WOS:000369837600012.

[16]M. Aspelmeyer, T. J. Kippenberg, and F. Marquardt, “Cavity optomechanics,” Reviews of Modern Physics **86**, 1391 (2014).

[17]P. Roelli, C. Galland, N. Piro, and T. J. Kippenberg, “Molecular cavity optomechanics as a theory of plasmon-enhanced raman scattering,” Nature nanotechnology **11**, 164–169 (2016).

[18]T. Ojanen and K. Børkje, “Ground-state cooling of mechanical motion in the unresolved sideband regime by use of optomechanically induced transparency,” Physical Review A **90**, 013824 (2014).

[19]R. Y. Chiao, R. W. Haun, N. A. Inan, B.-S. Kang, L. A. Martinez, S. J. Minter, G. A. Munoz, and D. A. Singleton, “A gravitational aharonov-bohm effect, and its connection to parametric oscillators and gravitational radiation,” in *Quantum Theory: A Two-Time Success Story* (Springer, 2014) pp. 213–246.

[20]Y. Ma, S. L. Danilishin, C. Zhao, H. Miao, W. Z. Korth, Y. Chen, R. L. Ward, and D. G. Blair, “Narrowing the filter-cavity bandwidth in gravitational-wave detectors via optomechanical interaction,” Physical review letters **113**, 151102 (2014).

[21]P. Bernard, G. Gemme, R. Parodi, and E. Picasso, “A detector of small harmonic displacements based on two coupled microwave cavities,” Review of Scientific Instruments **72**, 2428–2437 (2001).

[22]C. Reece, P. Reiner, and A. Melissinos, “Parametric converters for detection of small harmonic displacements,” Nuclear Instruments and Methods in Physics Research Section A: Accelerators, Spectrometers, Detectors and Associated Equipment **245**, 299–315 (1986).

[23]B. Vogell, B. Vermersch, T. Northup, B. Lanyon, and C. Muschik, “Deterministic quantum state transfer between remote qubits in cavities,” Quantum Science and Technology **2**, 045003 (2017).

[24]T. Brecht, W. Pfaff, C. Wang, Y. Chu, L. Frunzio, M. H. Devoret, and R. J. Schoelkopf, “Multilayer microwave integrated quantum circuits for scalable quantum computing,” npj Quantum Information **2**, 16002 (2016).

[25]X. Yao and L. Maleki, “Optoelectronic microwave oscillator,” Journal of the Optical Society of America B-Optical Physics **13**, 1725–1735 (1996), pT: J; TC: 578; UT: WOS:A1996VA92900011.

[26]M. Metcalfe, “Applications of cavity optomechanics,” Applied Physics Reviews **1**, 031105 (2014), pT: J; TC: 72; UT: WOS:000342814900005.

New Journal of Physics
The open access journal at the forefront of physics

Deutsche Physikalische Gesellschaft DPG IOP Institute of Physics

Electromagnetic coupling to centimeter-scale mechanical membrane resonators via RF cylindrical cavities

To cite this article: Luis A Martinez *et al* 2016 *New J. Phys.* **18** 113015

IOP Publishing New J. Phys. **18** (2016) 113015 doi:10.1088/1367-2630/18/11/113015

New Journal of Physics
The open access journal at the forefront of physics

Deutsche Physikalische Gesellschaft DPG
IOP Institute of Physics
Published in partnership with: Deutsche Physikalische Gesellschaft and the Institute of Physics

CrossMark

OPEN ACCESS

RECEIVED
2 May 2016

REVISED
17 October 2016

ACCEPTED FOR PUBLICATION
18 October 2016

PUBLISHED
8 November 2016

PAPER

Electromagnetic coupling to centimeter-scale mechanical membrane resonators via RF cylindrical cavities

Luis A Martinez[1], **Alessandro R Castelli, William Delmas, Jay E Sharping and Raymond Chiao**

Physics Department, University of California Merced, USA

[1] Author to whom any correspondence should be addressed.

E-mail: lmartinez35@ucmerced.edu

Keywords: RF cavity, optomechanics, Maxwell stress tensor, interferometry, thin membrane, mechanical modes, radiation pressure

Abstract

We present experimental and theoretical results for the excitation of a mechanical oscillator via radiation pressure with a room-temperature system employing a relatively low-(Q) centimeter-size mechanical oscillator coupled to a relatively low-Q standard three-dimensional radio-frequency (RF) cavity resonator. We describe the forces giving rise to optomechanical coupling using the Maxwell stress tensor and show that nanometer-scale displacements are possible and experimentally observable. The experimental system is composed of a 35 mm diameter silicon nitride membrane sputtered with a 300 nm gold conducting film and attached to the end of a RF copper cylindrical cavity. The RF cavity is operated in its TE_{011} mode and amplitude modulated on resonance with the fundamental drum modes of the membrane. Membrane motion is monitored using an unbalanced, non-zero optical path difference, optically filtered Michelson interferometer capable of measuring sub-nanometer displacements.

1. Introduction

We are entering a new realm of experimental quantum mechanics where it is possible to observe quantum-mechanical behavior in relatively large *mesoscale* objects. In recent years high-Q, high-frequency mechanical oscillators have emerged as platforms for quantum optomechanics, electromechanics, parametric amplifiers, phononic and nanomechanical systems [1–8]. The majority of optomechanical systems use high-finesse optical cavities, in which the underlying optomechanical coupling force is due to the radiation pressure arising from transverse-electromagnetic (TEM) modes in the optical cavity [9, 10]. More recently, microwave *cavity* optomechanics has shown great promise for the study of the coupling of electromagnetic energy and mechanical motion at the quantum level [11–13]. We emphasize that the term *cavity* is generally used in microwave *cavity* optomechanics to describe two-dimensional superconducting microstrip/co-planar waveguides, or one-dimensional transmission line resonator type architectures. Microwave *cavity* optomechanical systems operate at lower electromagnetic frequencies which reduces the magnitude of the optomechanical forces. However, significant couplings to micro-mechanical resonators can be achieved due to the small electromagnetic mode volumes achievable with such schemes [14].

In contrast, optomechanics with standard, macroscale (3D) RF cavities has not been an attractive avenue primarily because of the large electromagnetic mode volumes which may lead to weak coupling strengths [10, 14], and the lack of centimeter-size high-Q mechanical oscillators. For example, a theoretical estimate based on the frequency pull parameter ($G \equiv \mathrm{d}\omega/\mathrm{d}x = \pi^2c^2/\omega_{011}L^3$) of a 10 GHz cylindrical RF cavity operating in the TE_{011} mode yields an optomechanical coupling strength of $g_0/2\pi = Gx_{\mathrm{ZPF}} \sim 1 \times 10^{-6}$ Hz for the room temperature system presented here [9]. Yet, among the first experimentally optomechanical couplings explored were with three-dimensional RF cavities by Braginsky [15, 16], whose work on coupling a rectangular RF cavity to a pendulum ultimately lead to the optical spring effect and the field of optomechanics. The ongoing development of high-Q superconducting radio frequency (SRF) cavity resonators and macro-scale mechanical membrane oscillators [2] now motivate a natural platform for the study of macro-scale optomechanical systems.

Chemical surface treatments have now become rather standard in SRF cavities, and quality factors on the order of 100 million or above can be relatively easily achieved [17–21]. Thus, it is natural to envision macro-scale optomechanical systems consisting of SRF cavity resonators and macro-scale, high-Q, high-frequency mechanical oscillators. For example, an optomechanical system consisting of superfluid helium coupled to a SRF niobium cavity has been demonstrated [22]. Or more recently, microkelvin cooling of a millimeter-sized silicon nitride mechanical resonator coupled to a 3D aluminum superconducting microwave cavity was achieved [23].

In an effort to move towards SRF centimeter-scale cavity optomechanical systems, we present theoretical and experimental results which demonstrate that optomechanical couplings can be achieved with low-Q centimeter-size mechanical resonators coupled to the electromagnetic fields of RF cavities exhibiting relatively low Q-factors. The source of the optomechanical coupling is the radiation pressure which arises from transverse-magnetic (TM) or transverse-electric (TE) electromagnetic modes found in RF cavities. A centimeter-scale room temperature system with a relatively low-quality-factor mechanical oscillator coupled to a RF copper cylindrical cavity is used to experimentally confirm that the radiation pressure, due to the magnetic component of the Maxwell stress tensor in a cylindrical cavity, is sufficiently strong enough to excite the drum modes of a 35 mm diameter, 500 nm thick, silicon nitride membrane attached to one end of the cavity.

These results suggest that optomechanics with SRF microwave frequency cavities might hold promise for future systems which can exploit their extremely high Q-factors. We add that future configurations using membrane-SRF-cavities schemes might pave the way for macroscopic parametric amplifier/oscillator systems [24, 25], which could then be used to perform experiments probing the quantum/classical boundary. Finally, hybrid systems that coherently couple microwave fields to optical fields [26] and, therefore, efficiently transfer squeezed states from the microwave to the optical regime, might also be a feasible future application for such SRF cavity systems.

2. Calculations

2.1. Membrane coupling via magnetic component of Maxwell stress tensor in a cylindrical cavity

For a cylindrical cavity operating in a TE_{011} mode the relevant fields at the end-walls are the azimuthal component of the electric field $E_\phi \propto \sin(\pi z/L)$, the radial component of the magnetic field $H_\rho \propto \cos(\pi z/L)$, and the longitudinal component of the magnetic field $H_z \propto \sin(\pi z/L)$; where L is the length of the cavity, and z is along the axial direction. For perfect conductor boundary conditions the electric field component of the Maxwell stress tensor in the cylindrical cavity vanishes at the end-walls. However, the magnetic field components are at a maximum at the end-walls and dominate the pressure exerted on the membrane.

Now consider a large mechanical membrane attached at one end-wall of a cylindrical cavity (figure 2). We analyze the electromagnetic coupling with a thin circular silicon nitride membrane attached to one end of a cylindrical RF cavity of radius R. For this calculation, the cavity is assumed to be excited in its resonant TE_{011} mode which sets up an azimuthally symmetric electromagnetic pressure on the silicon nitride membrane. The boundary conditions of the conductor, cavity geometry, and membrane (clamped boundary) are assumed to be ideal. This procedure can be generalized to other cavity modes [27].

The displacement (u) for the damped-driven elastic membrane is given by the following equation of motion [28]

$$\rho\ddot{u} + \gamma\dot{u} - \mathcal{T}\nabla^2 u = \mathrm{e}^{\mathrm{i}\Omega t}F(r), \tag{1}$$

where ρ is the mass per unit area of the membrane (assumed to be uniform), $\gamma \equiv 2\rho\beta$ is the damping coefficient, $\mathcal{T}$ is the tension per unit length, Ω is the modulation driving frequency, and $F(r)$ is an azimuthally symmetric driving pressure. The particular solution to equation (1) is obtained via a Bessel-series solution method with the following anzatz[2]

$$u(r,\, t) = \mathrm{e}^{\mathrm{i}\Omega t}\sum_{n=1}^{\infty} A_n J_0\left(x_{0n}\frac{r}{R}\right), \tag{2}$$

where J_0 is the zero order Bessel function, x_{0n} is the nth zero of the zeroth order Bessel function, and R is the radius of the membrane which is assumed to coincide with the radius of the RF cylindrical cavity.

The force per unit area along the normal direction on the membrane is computed from the Maxwell stress tensor T_{ij} [29]

---

[2] Clamped boundary conditions, $u(r = R,\, \theta) = 0$.

$$T_{ij} = \epsilon_0\left(\mathcal{E}_i\mathcal{E}_j - \frac{1}{2}\delta_{ij}\mathcal{E}^2\right) + \frac{1}{\mu_0}\left(\mathcal{B}_i\mathcal{B}_j - \frac{1}{2}\delta_{ij}\mathcal{B}^2\right), \tag{3}$$

where the $\mathcal{E}$ and $\mathcal{B}$ fields are those of a cylindrical cavity TE_{011} mode which are readily obtainable [19, 30]. For the TE_{011} mode, the force per unit area along the normal direction on the membrane is

$$T_{zz} = \frac{\mu_0\mathcal{H}_0^2}{2}[J_1^2(k'_{01}r)], \tag{4}$$

where $k'_{0n} = x'_{0n}/R$ is the nth zero of the derivative of the zeroth order Bessel function $J'_0(x)$, and $\mathcal{H}_0$ is the peak magnetic field strength inside the cavity. Since the driving force along the normal direction ($F(r)$) is proportional to T_{zz}, we write the driving pressure on the membrane as

$$F(r) \equiv -\frac{1}{2}\frac{\mu_0\mathcal{H}_0^2}{2}\left[J_1^2\left(x'_{01}\frac{r}{R}\right)\right], \tag{5}$$

where we have included an extra factor of $1/2$ for the time averaging of the fast oscillating RF frequency (ω_{011}). This is because the RF power is amplitude modulated at the low acoustical frequency Ω, which drives the membrane at resonance.

We compute $F(r)$ as a Bessel series [31] and calculate the coefficients numerically. The particular solution for the membrane's displacement is[3]

$$u(r, t) = \mathrm{e}^{\mathrm{i}\Omega t+\mathrm{i}\phi}\sum_{n=1}^{\infty}A_nJ_0\left(x_{0n}\frac{r}{R}\right), \quad \text{with} \tag{6}$$

$$A_n = \frac{\mu_0\mathcal{H}_0^2}{\rho}\frac{c_n}{\sqrt{(\omega_{0n}^2 - \Omega^2)^2 + 4\beta^2\Omega^2}}, \quad \text{and} \tag{7}$$

$$c_n = \frac{\int_0^1 \zeta\, J_1^2(x_{11}\zeta)J_0(x_{0n}\zeta)\mathrm{d}\zeta}{J_1^2(x_{0n})}, \tag{8}$$

where ρ is the mass per unit area, ϕ is a phase factor, β is the HWHM decay rate of the membrane's resonance in angular units, $\mathcal{H}_0 \equiv H_0(\pi R/Lx_{11})$ with H_0 the peak magnetic field inside the cavity [27], and $\zeta \equiv r/R$ is a dimensionless integration variable. Because we have assumed an azimuthally symmetric driving force, the solution is restricted to azimuthally symmetric mechanical drum modes with eigenfrequencies of the form ω_{0n}. However, as with any mechanical resonator all natural modes can be excited and in general all natural drum modes should be observable near their natural resonances

$$\omega_{mn} = \frac{x_{mn}v}{R}, \tag{9}$$

where v is the speed of sound for transverse vibrations of the silicon nitride membrane, and x_{mn} are the mth zeros of the nth order Bessel function.

2.2. Displacement amplitude estimate

This calculation serves as an order of magnitude estimate of the displacement because the silicon nitride membrane is a composite structure whose mechanical properties are difficult to fully describe analytically, hence, several simplifications have been made: (1) the effective-mass is assumed equivalent to the sum of the 500 nm silicon nitride window mass and the 300 nm gold-film mass. (2) The effects of the elastic properties of the 300 nm gold film on the 500 nm silicon nitride membrane are not considered. (3) Ideal clamped-boundary conditions are assumed for the membrane which are difficult to achieve in practice. And (4) it does not consider the effects of the 500 μm annular silicon frame which also has its own set of mechanical resonances and boundary conditions. Lastly, we emphasize that our linear harmonic oscillator model does not incorporate any nonlinear effects that might arise, for example, from a quadratic drag term. With this in mind, an estimate for the maximum displacement at the center of the membrane ($r = 0$) follows from equations (6)–(8)

$$u_{\max} \approx \frac{15P_f Q_{0\mathrm{RF}}}{mf_{011}}\sum_n\frac{c_n}{\sqrt{(\omega_n^2 - \Omega^2)^2 + 4\beta^2\Omega^2}}, \tag{10}$$

where we have assumed perfect power coupling to the RF cavity, $Q_{0\mathrm{RF}}$ is the cavity's internal Q factor, P_f is the RF forward traveling power, and m is the assumed effective-mass of the membrane. When the membrane is driven at its fundamental resonance with $m = 10$ mg, $P_\mathrm{f} = 25$ mW, $Q_{0\mathrm{RF}} = 20,000$, $\omega_{011} = 2\pi \times 10.332$ GHz,

---

[3] In the simplification of this solution the following Bessel relations were used; $J_2(x) = 2J_1(x)/x - J_0(x)$, and $\int_0^1 zJ_0^2(x_{0n}z)\mathrm{d}z = J_1^2(x_{0n})/2$, where x_{0n} is the nth zero of the zeroth order Bessel function.

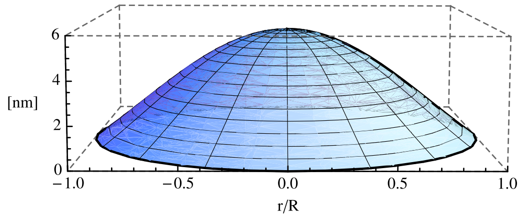

Figure 1. The Bessel series solution, equation (6), plotted when driven at the fundamental resonance, for the first 20 terms in the series. Parameters in the text.

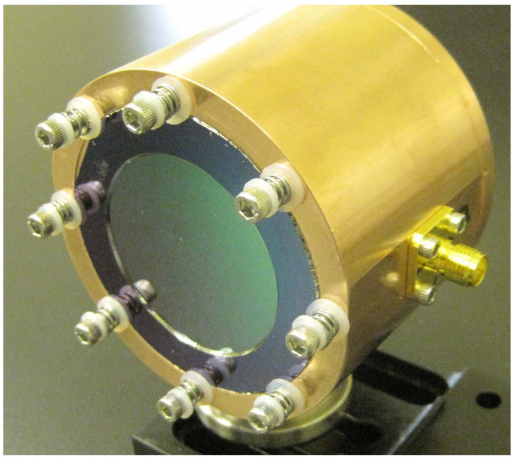

Figure 2. Experimental configuration of copper cavity with silicon nitride membrane attached.

$\beta = 2\pi \times 10$ Hz, and $\Omega = 2\pi \times 5,878$ Hz, we find $u_{\max} \sim 6.0$ nm. A plot of the solution for the first 20 terms in the series of the membrane driven at the first resonance with the given parameters is plotted in figure 1.

3. Experiment

The experiment used a cylindrical cavity made from high purity oxygen free copper excited in its TE_{011} mode and a 35 mm diameter, 500 nm thick silicon nitride membrane acquired from Norcada. The membrane was sputtered with a 300 nm gold film and attached to one end of the cavity (figure 2). Excitation of the membrane's mechanical modes was achieved by amplitude modulation of the cavity's input power at a frequency Ω. Modulation of the RF input power directly modulates the radiation pressure on the silicon nitride membrane, thus exciting the fundamental drum mode resonances of the membrane.

3.1. The RF cylindrical cavity

Measurement of the RF resonant frequencies and Q-factor were made with an HP 8720C Network Analyzer. Figure 3 shows a typical S11 reflection measurement on our copper cylindrical cavity with $D = 3.81$ cm and overall length of 4.229 cm, however, the relevant internal length was $L = 3.81$ cm. The RF cavity was designed with a $D/L = 1$ ratio and a resonance at 10.332 GHz for the TE_{011} mode. A small gap in the solid end-cap shifts the degenerate TM_{111} mode. Measurement of the cavity's loaded (external) Q-factor was determined experimentally from $Q_{\mathrm{L}} = f/2\Delta f$, where Δf is the HWHM value at the resonant frequency. The loaded quality factor of the copper cavity with the gold silicon nitride membrane attached at one end was 10 400 $\pm$ 5% and slightly undercoupled with a coupling coefficient of 0.9.

3.2. Low-frequency membrane displacement measurement

Sub-nanometer displacement measurements using Michelson interferometers have been well studied and play an important role in the study of piezoelectric devices [32–35]. Here we employ an unbalanced, non-zero optical path difference Michelson interferometer for the membrane's displacement measurement. We implement the use of an optical filter via a single mode fiber optic to avoid interference pattern distortions caused by poor reflection quality from the coated membrane, and to compensate for the non-zero optical path difference. Noise

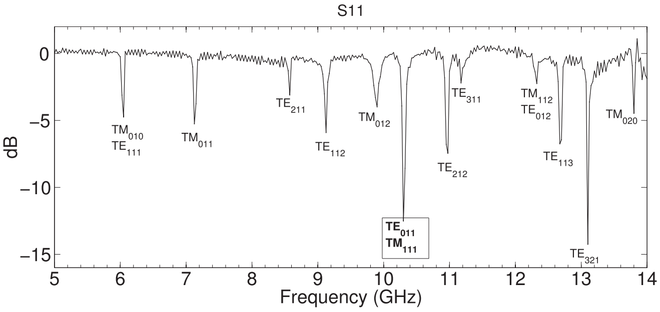

Figure 3. S11 measurement showing the resonant frequencies of the copper cavity with a gold coated silicon nitride window at one end. The TE$_{011}$ mode resonance frequency is 10.332 GHz. The degenerate TM$_{111}$ is slightly shifted by adding a small gap at the end-cap of the RF cavity. The relevant dimensions are $D = 3.81$ and $L = 3.81$ cm.

reduction is achieved by placing the interferometer inside a ~7 mbar vacuum chamber pumped down with a roughing pump. This scheme provides high sensitivity and easy set up, but the major limitations are ambient vibrational and acoustical noise.

For conversion of the light intensity to a voltage we use a Thorlabs FDS 100 Si photodiode detector in a photoconductive mode. In this configuration the output voltage of the photodiode detector scales linearly with the intensity and the voltage signal is independent of the responsivity of the detector, thus, eliminating the need for a calibrated photodetector.

The displacement amplitude (x_0) for a Michelson interferometry scheme can be extracted from

$$x_0 = \frac{\sqrt{2}\, V_s[\mathrm{rms}]\, \lambda}{4\pi\sqrt{\Delta V_1 \Delta V_2}\, \sin(2kd)}, \tag{11}$$

where $kx_0 \ll 1$, λ is the laser wavelength, d is the DC optical path difference, and $\Delta V_{1,2}$ are the voltages of each arm of the interferometer. Note that the voltages ΔV_1 and ΔV_2 are measured relative to the DC offset voltage of the detector when no light is incident. The optical phase added by the DC optical path difference is tuned via a piezoelectric actuator prior to any modulation so that $\sin(2kd) = 1$. This occurs when the total voltage is equal to the sum of the individual voltages from each arm of the interferometer; $\Delta V = \Delta V_1 + \Delta V_2$. After proper tuning, the displacement of the membrane is extracted from a measurement of the DC and rms voltages from equation (11) with $\sin(2kd) = 1$.

Measurements were performed with a 10 mW helium–neon 633 nm laser as the light source. The DC voltages (ΔV_1 and ΔV_2) were measured with an oscilloscope. Solenoid-actuated blockers were used to block the beams as necessary to measure each arm's intensity. A piezo-electric actuator was used to tune the interference pattern to its most sensitive setting as described above. The rms voltage was measured with an SRS 830 DSP lock-in amplifier, and the lock-in reference signal was used to amplitude modulate the Agilent N5183A RF signal generator at the reference frequency. A Labview *VI* program automatically swept the reference frequency and recorded the rms voltage measurement from the lock-in. Since the measurements can be done relatively quickly, no feedback loop was implemented (figure 4).

4. Results and discussion

The resonant frequencies of the mechanical drum modes are theoretically calculated from equation (9). We use the experimentally determined value of the first resonance as a reference point for calculating the expected resonant frequencies of the higher order modes. That is, $\omega_{11} = \omega_{01}x_{11}/x_{01}$, where ω_{01} is experimentally determined, etc. The gold-coated silicon nitride membrane's fundamental resonance was experimentally observed at 5878 Hz. Based on this value the second (x_{11}), third (x_{21}), and fourth (x_{02}) modes are expected at 9366, 12 554, and 13 493 Hz, respectively. The second drum mode was experimentally measured at 9380 Hz (figure 5). The third mode was observed at approximately 12 700 Hz which is also in good agreement with the expected theoretical resonance value. Finally, the fourth mode was not discernible due to the numerous signals/resonances detected in the range from 13 500–14 200 Hz (figure 5).

Figure 6 shows the experimental data for the first mode at 5878 Hz for different RF forward traveling powers. The solid curves are fits to equations (6)–(8) from which we extract the resonance frequency and quality factor. Equation (11) is used to determine the membrane's vibration amplitude. A maximum vibration amplitude of approximately 0.9 nm was observed which is consistent with the order of magnitude estimate of 6 nm. To confirm excitation of the main resonance, we varied the RF forward traveling power. From equation (10) we see

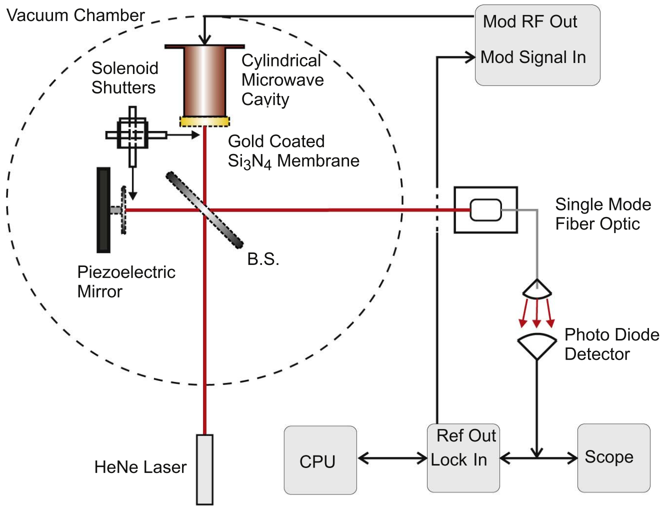

Figure 4. Experimental configuration for membrane displacement measurement.

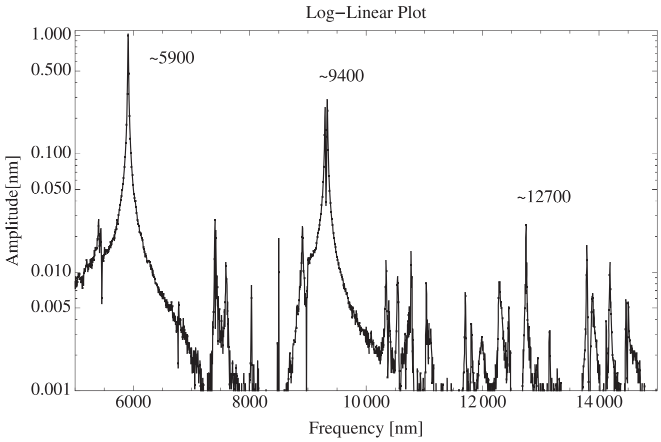

Figure 5. Log-linear spectrum plot from 5000–15 000 Hz shows the detected modes. The first two resonances at ~5900 and ~9400 Hz correspond to the first two fundamental drum modes; the third mode is observed near 12 700 Hz. The fourth mode is hard to discern since there are several other peaks detected in the relevant region.

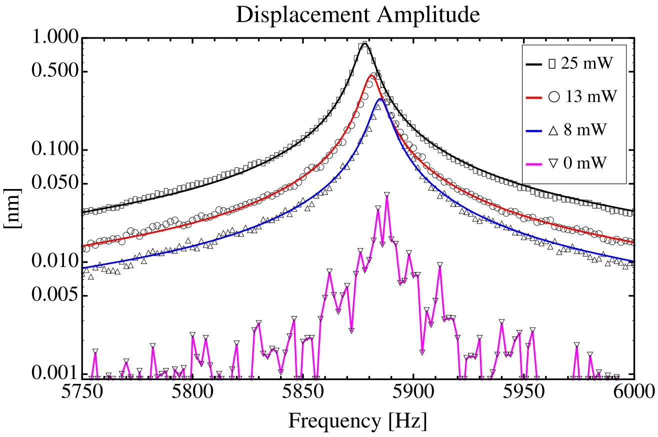

Figure 6. Log-linear plot of experimental data and fits to equation (6) (solid curves) for different RF powers of the TE_{011} mode. For 25 mW of forward traveling power the membrane's displacement amplitude is approximately 0.9 nm at its resonance frequency of 5878 Hz.

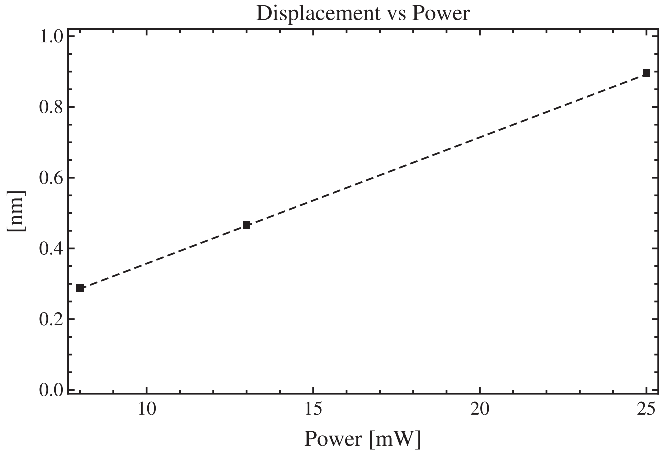

Figure 7. Membrane displacement amplitude plotted against RF forward traveling power. The dash line is a linear fit to the experimentally measured values. The error bars are smaller than the sizes of the square data points.

that the power scales linearly with the amplitude of oscillation of the membrane. This linear relationship is displayed in figure 7. The mechanical *Q* of the membrane is calculated from the experimental results and is $Q_M \approx 300$.

It was observed that the resonance frequency of the membrane slightly decreased as the RF power was increased. The observed shift in frequency is on the order of 4–10 Hz as seen in figure 6. Note that during actual measurements the vacuum pump was shut off to reduce vibrational noise which lead to a gradual pressure increase during the experimental runs. We speculate that the frequency-shift may be due to viscous damping associated with air resistance (drag) and/or the DC force created by the electromagnetic fields in the RF cavity. Based on the damped driven linear oscillator model used, the observed frequency-shift as a function of power is not expected in the solution since it does not include the DC component of electromagnetic force or account for any nonlinear effects. Thus, nonlinear effects should not be ruled out, and may be investigated further. However, to test the effects of viscous damping due to increased air pressure, the air pressure of the chamber was increased and the relevant excited drum modes were observed to decrease in frequency. This behavior is consistent with the solution of a damped-driven linear oscillator. Finally, we add that the excitation of the membrane resonance was confirmed using an acoustical measurement with a speaker tuned to the main fundamental resonant frequency.

5. Conclusions and future work

We demonstrated that a copper cylindrical microwave cavity with a loaded *Q* of 10 400 can drive into motion a 35 mm diameter, 500 nm thick silicon nitride membrane coated with a 300 nm gold film placed at one end. The driving mechanism is dominated by the magnetic field pressure of the radio frequency electromagnetic fields exerted on the membrane as described by Maxwell’s stress tensor. This work demonstrates that radio frequency electromagnetic fields of traditional RF cavities can couple to macroscopic mechanical oscillators even in room temperature situations with low powers and relatively low *Q*’s.

Indeed, couplings with three-dimensional RF cavities can be achieved when the size of the mechanical resonator becomes comparable with the size of the cavity resonator. Future direction of this work includes using a high-*Q* SRF cavity coupled to a centimeter-sized mechanical resonator consisting of a flexible superconducting niobium coated membrane. Stronger couplings are expected since the forces scale with resonator quality factors. Such three-dimensional macroscopic configurations seem to be a natural direction away from the currently used two-dimensional micro-sized architectures in optomechanics. Three-dimensional architectures lead naturally to much higher quality-factor cavities, since the surface current densities are much lower due to the much smaller surface-to-volume ratios of such 3D microwave cavities as that illustrated in figure 2. To test such a scheme we would like to excite higher frequency dilatational modes as observed in [5], but with high-Q SRF cavities instead of high repetition lasers.

Acknowledgments

We thank Bong-Soo Kang, Jeremias Gonzales, Jacob Pate, Johnathon Thompson, Nathan Inan, Edward Silva, for their help and support on this project. We acknowledge Robert Haun for his dedicated help in the beginning stages of this work. This work was supported in part by the Defense Advanced Research Projects Agency (DARPA) under contract W911NF-14-C-0061. The views, opinions, and/or findings expressed are those of the author(s) and should not be interpreted as representing the official views or policies of the Department of Defense or the U S Government.

References

[1] Peterson R W, Purdy T P, Kampel N S, Andrews R W, Yu P-L, Lehnert K W and Regal C A 2016 *Phys. Rev. Lett.* **116** 063601
[2] Yuan M, Cohen M A and Steele G A 2015 *Appl. Phys. Lett.* **107** 263501
[3] Marquardt F and Girvin S M 2009 *Trend: Optomechanics. Physics* **2** 40
[4] Thompson J D, Zwickl B M, Jayich A M, Marquardt F, Garvin S M and Harris J G E 2008 *Nature* **452** 72
[5] Bruchhausen A *et al* 2011 *Phy. Rev. Lett.* **106** 077401
[6] Hatanaka D, Mahboob I, Onomitsu K and Yamaguchi H 2013 *App. Phy. Lett.* **102** 213102
[7] Palomaki T, Teufel J, Simmonds R and Lehnert K 2013 *Science* **342** 710
[8] Bagci T *et al* 2014 *Nature* **507** 81
[9] Aspelmeyer M, Kippenberg T J and Marquardt F 2014 *Rev. Mod. Phys.* **86** 1391
[10] Regal C and Lehnert K 2011 *J. Phys.: Conf. Ser.* **264** 012025
[11] Teufel J, Lecocq F and Simmonds R 2016 *Phys. Rev. Lett.* **116** 013602
[12] Regal C, Teufel J and Lehnert K 2008 *Nat. Phys.* **4** 555
[13] Teufel J, Harlow J, Regal C and Lehnert K 2008 *Phys. Rev. Lett.* **101** 197203
[14] Aspelmeyer M, Kippenberg T J and Marquardt F 2014 *Cavity Optomechanics: Nano-and Micromechanical Resonators Interacting With Light* (Berlin: Springer)
[15] Braginskii V B, Manukin A B and Tikhonov M Y 1967 *JETP* **25** 653
[16] Braginskii V B, Manukin A B and Tikhonov M Y 1970 *JETP* **31** 829
[17] Turneaure J and Weissman I 1968 *J. Appl. Phys.* **39** 4417
[18] Ciovati G 2006 *Physica* C **441** 44
[19] Padamsee H, Knoblock J and Hays T 2008 *RF Superconductivity for Accelerators* (Weinheim: Wiley)
[20] Kuhr S *et al* 2007 *App.Phy. Lett.* **90** 16410
[21] Reagor M *et al* 2013 *App. Phys. Lett.* **102** 192604
[22] De Lorenzo L and Schwab K 2014 *New J. Phys.* **16** 113020
[23] Yuan M, Singh V, Blanter Y M and Steele G A 2015 *Nat. Commun.* **6** 8491
[24] Chiao R Y, Martinez L A, Minter S J and Trubarov A 2012 *Phys. Scr.* **2012** 014073
[25] Chiao R, Haun R, Inan N, Kang B-S, Martinez L, Minter S, Munoz G and Singleton D 2014 *Quantum Theory: A Two-Time Success Story* ed D C Struppa and J M Tollaksen (Milan: Springer) pp 213–46
[26] Andrews R W, Peterson R W, Purdy T P, Cicak K, Simmonds R W, Regal C A and Lehnert K W 2014 *Nat. Phys.* **10** 321-6
[27] Martinez L A 2014 PQDT 1629463635
[28] Rao S S 2007 *Vibration of Continuous Systems* (Hoboken, NJ: Wiley)
[29] Griffiths D J 1999 *Introduction to Electrodynamics* 3rd edn (Upper Saddle River, NJ: Prentice-Hall)
[30] Wilson I, Schramm C and Kinzer J 1946 *Bell Syst. Tech. J.* **3** 408-43
[31] Watson G N 1966 *A Treatise on the Theory of Bessel Functions* 2nd edn (Cambridge: Cambridge University Press)
[32] Kholkin A L, Wütchrich C, Taylor D V and Setter N 1996 *Rev. Sci. Instrum.* **67** 1935
[33] Li J-F, Moses P and Viehland D 1995 *Rev. Sci. Instrum.* **66** 215
[34] Zhang Q M, Pan W Y and Cross L E 1987 *J. Appl. Phys.* **63** 2492
[35] Sizgoric S and Gundjian A A 1969 *Proc. IEEE* **57** 1312

AIP Advances

Electrostatic tuning of mechanical and microwave resonances in 3D superconducting radio frequency cavities

Cite as: AIP Advances **8**, 115223 (2018); https://doi.org/10.1063/1.5055887
Submitted: 11 September 2018 . Accepted: 12 November 2018 . Published Online: 27 November 2018

Jacob M. Pate, Luis A. Martinez, Johnathon J. Thompson, Raymond Y. Chiao, and Jay E. Sharping

AIP Advances **8**, 115223 (2018); https://doi.org/10.1063/1.5055887 **8**, 115223

AIP ADVANCES **8**, 115223 (2018)

Electrostatic tuning of mechanical and microwave resonances in 3D superconducting radio frequency cavities

Jacob M. Pate,[a] Luis A. Martinez, Johnathon J. Thompson,
Raymond Y. Chiao, and Jay E. Sharping
School of Natural Sciences, University of California Merced, Merced, California 95343, USA

(Received 11 September 2018; accepted 12 November 2018;

We implement a non-contact, external method of simultaneously fine-tuning a mechanical resonator and a superconducting radio frequency (SRF) cavity using a capacitor formed between a silicon nitride membrane and a copper electrode at cryogenic temperatures. The silicon nitride membrane forms a variable boundary condition for the SRF cavity thereby creating the optomechanical cavity. By controlling the DC voltage applied between an external electrode and the silicon nitride membrane we are capable of tuning the resonance frequency internal to the SRF cavity up to 25 kHz for a cavity with loaded quality factor of 2.5 million, corresponding to six cavity linewidths. At the same time we observe the electrostatic frequency shift of the membrane. This approach has the unique benefit of avoiding any dielectric insertion or added gaps due to a moving end-wall thereby limiting the loss of the cavity. Furthermore, this design avoids applied pressure typically used with piezoelectric devices in accelerator cavities. This work seeks to have strong impact in tuning high-Q cavities due to its ability to maintain low losses. https://doi.org/10.1063/1.5055887

I. INTRODUCTION

Superconducting radio frequency (SRF) cavities today are capable of achieving extraordinarily high quality factors $Q > 10^{11}$.[1–4] Moreover, three-dimensional SRF cavities have been shown to be an attractive platform for cavity optomechanics and quantum information.[5] Mechanical resonators in optomechanical cavities act as transducers for quantum systems in hybrid architectures, such as frequency conversion between microwave and optical light.[6,7] In recent years the field of cavity optomechanics has grown from observing radiation pressure in single cavities[8] to making use of multiple cavities with coupled modes for applications such as filters and locked references.[9–13]

The development of macroscopic 3D optomechanical cavities for quantum information is proving to be promising despite low optomechanical coupling rates.[14] State of the art 3D microwave cavities for quantum information typically have lifetimes on the order of milliseconds.[5] Strong coupling between a Josephson junction qubit and a macroscopic cavity has been achieved through the use of antennae.[15] Elsewhere, groups have used low loss silicon nitride membranes as mechanical resonators to achieve high cooperativity and strong electromechanical coupling between the mechanical oscillator and a cavity.[16–18]

In order to take advantage of the narrowband resonance of the cavity, one must be able to tune the frequency as desired. The challenge of introducing a tunable "in-situ" element can easily result in a degradation of the quality factor. Most often the method of frequency translation is achieved via a moving boundary condition, insertion of a dielectric element, or even applied strain on a

---

[a] Electronic mail: jpate@ucmerced.edu

resonator.[19–21] In the case of very high-Q resonators these techniques become challenging due to dielectric losses[22] or resistive losses when the tuning element is what perturbs the cavity mode.

We aim to construct a macroscopic platform for observing cavity electro- and optomechanical phenomena.[9,13,23–27] Specifically, this project enables the possibility of cooling macroscopic mechanical oscillators in the presence of low frequency noise.[28,29] Here, we use a non-contact, non-invasive method of tuning a superconducting radio frequency cavity using a capacitively-coupled mechanical oscillator acting as an end-wall boundary to the cavity. We have performed experiments on two different cavities with loaded quality factors of $Q_L = 1.1 \times 10^6$ and $Q_L = 2.5 \times 10^6$ for cavities A and B, respectively. For the higher-Q cavity presented in this work, the tuning range was observed to be about 25 kHz with the potential for much larger range for the present cavity geometry.

We couple to the TE_{011} mode because the field amplitude is small where the membrane meets the cavity wall. This mode maximizes Q. We adjust the resonance frequency of the TE_{011} mode for a SRF cavity through the movement of the center of mass displacement of the mechanical oscillator (see Fig. 1). One end-wall of the SRF cavity is composed of a silicon nitride membrane (acting as the mechanical oscillator) with niobium deposited on the underside. On the outside of the cavity, we have machined two electrodes that capacitively couple to the membrane. The membrane forms one side of the variable capacitor while the other side is a gold-plated copper electrode.

It is worth noting that the use of a flexible boundary is by no means a new concept. In fact, one of the first uses dates back to Theremin's microwave resonator used for spy purposes[30] wherein acoustic waves incident on a thin metallic disk modulated a cavity resonance frequency. In this manner, a tuning post was used to achieve larger coupling between the metallic disk and the microwave field. More recently, a group has used a thin diaphragm consisting of a gold-coated silicon-on-insulator wafer to electrically tune a room temperature microwave cavity.[31] Other groups have used piezoelectric devices to shift the resonance frequency by pushing on a cavity boundary.[32] In particle accelerators a combination of piezoelectric crystals and stepper motors are used to tune the frequency of accelerator cavities up to 250 kHz in bandwidth.[33–35] By comparison, ours is a non-contact approach for tuning SRF cavities at cryogenic temperatures where the frequency resolution is limited by the resolution and stability of the applied voltage.

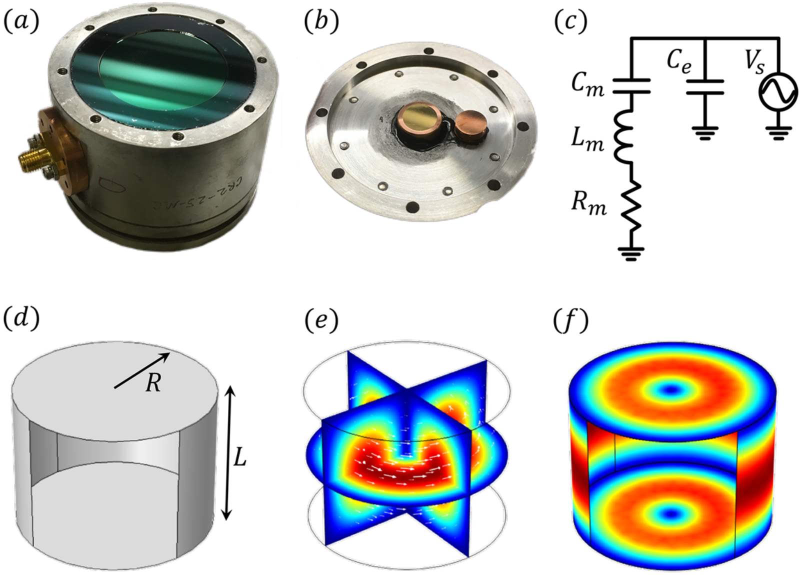

FIG. 1. (a) Image of the SRF cavity with the silicon nitride membrane. The antennae are anchored to the niobium body with copper adapters. (b) Image of the electrodes epoxied to the aluminum bracket. The sensing electrode is 8.7 mm in diameter while the driving electrode is 12.5 mm in diameter. The bracket flips over and attaches to the body of cavity with corresponding threaded holes. (c) The electrical model[13] of the mechanical resonator (C_m, L_m, and R_m) and capacitance C_e formed between the copper electrode and the membrane with source voltage V_s. (d) Geometric model of the cylindrical cavity. (e) Electric field multislice of the TE_{011} mode. (f) Magnetic field surface plot of the TE_{011} mode.

II. MECHANICAL OSCILLATOR MODEL

There is a frequency shift in the membrane resonance that is best understood as the "spring-softening" effect commonly seen in the NEMS and MEMS community.[36,37] As the membrane flexes from the applied force, the internal SRF cavity length is slightly increased leading to a RF frequency decrease as $\omega_0 \propto L^{-1}$. In order to illustrate the simple electrostatic effect of a capacitor, we introduce the potential energy of a capacitor having variable capacitance $C(x)$ with AC and DC voltage components, $U = \frac{1}{2}C(x)(V_{DC} + V_{AC}\cos(\omega t))^2$.

We assume the membrane displacement x is much smaller than the separation distance d, $x \ll d$, which allows the force acting on the membrane to be expressed as $F_c \approx \frac{1}{2}\frac{C_0}{d}\left(1 - \frac{2x}{d}\right)V_{DC}^2$. Also, due to the smallness of V_{AC}, we approximate the second and third cross terms as negligible in comparison to the static DC component. Furthermore, we assume the spring constant is dominated by a mechanical and an electrical component $k_{\text{eff}} \equiv k_{\text{mech}} - k_{\text{elec}}$. Therefore we make an expansion of the resonance frequency of the mechanical oscillator.

$$\Omega_m \approx \sqrt{\frac{k_{\text{mech}}}{m}}\left(1 + \frac{1}{2}\frac{k_{\text{elec}}}{k_{\text{mech}}}\right) \tag{1}$$

This leads to a fractional shift in the mechanical frequency due to the electrical force of the electrode pulling the membrane.

$$\frac{\delta\Omega_m}{\Omega_m} \approx \frac{1}{2}\frac{k_{\text{elec}}}{k_{\text{mech}}} = -\frac{\epsilon A}{2d^3 k_{\text{mech}}}V_{DC}^2 \tag{2}$$

Perhaps most important about this equation is the dependence on the distance between the membrane and electrode to the third power. Though it is beyond the scope of this paper to examine in depth theoretically, the SRF frequency shift is dependent upon the overlap of the mechanical mode displacement profile and the TE_{011} mode.

III. SYSTEM IMPLEMENTATION

Referring to Fig. 1, the SRF cavity is machined from superconducting grade niobium RRR > 300 in two separate pieces, a cylindrical body and an end-cap. The construction of the end-wall and cylindrical body allows for future modular designs in which multiple cavities can be assembled. The drawback of this cavity design is the gap between the cylindrical body and the end-wall, which increases the surface resistance as the surface currents are inhibited across this gap. The cavity has diameter and length equal to 38.1 mm, which produces a resonance frequency of $\omega_0/2\pi = 10.3$ GHz for the TE_{011} mode.

Coupling to the SRF mode is made possible using a loop antenna at the center of the cavity. The cavity has been chemically etched after machining using the standard buffered-chemical-polish treatment.[38] No heat treatment was needed or used for these experiments because the goal was to focus on the frequency tuning mechanism rather than to optimize Q.

The cavity is placed in a dilution refrigerator and held at a temperature of approximately $T = 65$ mK. Two semi-flexible stainless steel SMA cables going down into the fridge are devoted to the acoustic measurements of the membrane while the others are used for microwave transmission and reflection measurements of the cavities. The transmission output of the cavity is sent to a HEMT amplifier at the 4K plate and further amplified at room temperature with two smaller post-amplifiers.

The aluminum bracket on the outside of the cavity houses the two electrodes and is secured to the SRF cavity body using brass 4-40 screws (see Fig. 1). The gold-coated electrode mounted in the center of the bracket is referred to as the driving electrode. The electrode that is off-center and slightly smaller is the sensing electrode. Both copper electrodes were secured in place using Stycast 2850 epoxy for electrical insulation and thermal conduction. Grooves were cut into the outer body of the copper electrodes to ensure the epoxy would firmly adhere to the copper in order to prevent any movement that would result in an electrical short or destruction of the membrane. The driving electrode was placed approximately 170 μm away (see Fig. 3) from the membrane while the sensing electrode is roughly double the distance. A bronze-shim (0.005" thick) was made into a spring washer to apply pressure on the silicon frame of the membrane. The membrane window is 38.1 mm in diameter and 800 nm thick (500 nm silicon nitride and 300 nm deposited niobium).

IV. RESULTS

For the purpose of *finding* the narrowband mechanical resonance signal (before shifting the resonance) arising from the sensing electrode and limiting cross-talk between the two copper electrodes, one can look at the force acting on the membrane and the cross term $\propto V_{AC}V_{DC}$. We keep the force term constant by simultaneously increasing the DC bias while decreasing the AC drive. Since the noise is AC-coupled, this naturally leads to an increase of the signal to noise ratio. We refer to the DC driving voltage as the static voltage applied to the membrane to shift the frequency, not to be confused with a DC bias applied to the preamplifier circuit for the purpose of increasing sensitivity.

We estimate the cable capacitance to be roughly 250 pF, which is much larger than the source capacitance of 7 pF leading to a signal reduction of about 35. As a result of this we developed a preamplifier to pick up the small signal. We obtain a voltage noise level down to 1.5 nV/Hz$^{1/2}$ at a frequency of 10 kHz with a custom preamplifier delivered by Sierra Amps, LLC.

We measure the output acoustic signal from the amplifier chain on a lock-in amplifier while stepping the weaker AC-driving source with a function generator. The mechanical response of the membrane displays a Fano-like resonance for any single trace in Fig. 2 and is described by the following equation.[39]

$$V_{\text{meas}} = \frac{V_0}{1 - 2iQ_m \frac{\Omega - \Omega_m}{\Omega_m}} + \alpha e^{i\phi} \tag{3}$$

We have used the notation that V_0 is a scaling factor, $\Omega_m/2\pi$ is the mechanical resonance frequency, Q_m is the mechanical quality factor, and $\alpha e^{i\phi}$ is an offset that leads to the Fano-lineshape. The (0,1) resonance of the mechanical oscillator refers to the fundamental mode of a circular drum, or membrane. The results presented in Fig. 2 display the measured data as well as the fits according to Eq. 3, with V_0, Ω_m, Q_m, and $\alpha e^{i\phi}$ as fitting parameters. Although not displayed graphically, Q_m drops linearly with increasing DC driving voltage beyond 50 V. The room temperature mechanical quality factor for the (0,2) membrane mode was $Q_m \approx 1.1 \times 10^4$ at a low DC driving voltage and drops to $Q_m \approx 8.9 \times 10^3$ at the largest applied DC voltage.

In Fig. 2 and Fig. 3 the mechanical resonance data were taken at room temperature inside a dilution refrigerator at a pressure of 1×10^{-3} mbar. During fridge operation, the low frequency pulse-tube cooler and turbo pumps distort the signal by vastly raising the noise floor (see inset in Fig. 2). For this reason it is challenging to obtain low-noise, low-frequency data of the sample. To obtain cryogenic data from the mechanical oscillator one must modify the dilution refrigerator to incorporate a mass

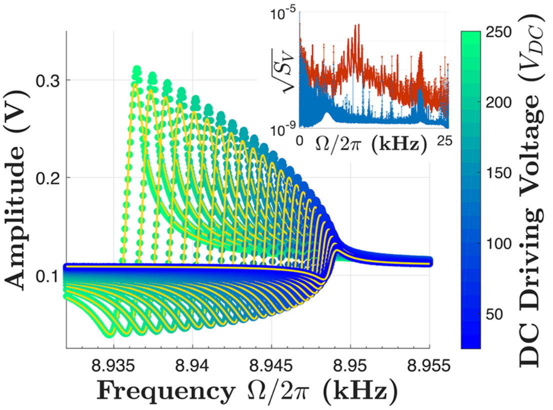

FIG. 2. Room temperature data showing the electrostatic frequency shift of the mechanical oscillator for the (0,2) mode. The dots are the data and the solid orange lines are theoretical fits to the data. The amplitude increases with a corresponding increase in the DC drive and resembles a Fano-like resonance. The inset represents the noise voltage in units of V/Hz$^{1/2}$ where the red data corresponds to the fridge in operation and blue data represents the fridge turned off.

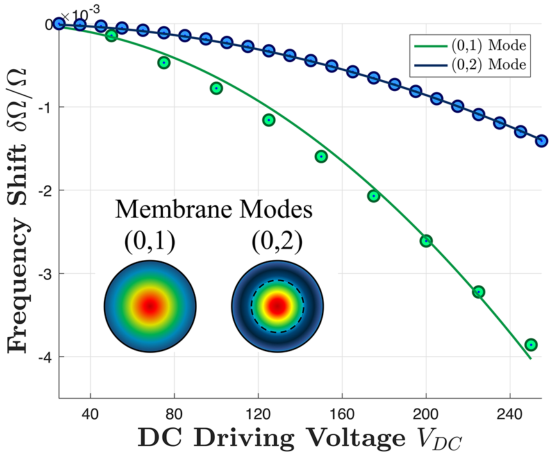

FIG. 3. The observed room temperature frequency shifts for the (0,1) and (0,2) membrane modes for cavity A are plotted as a function of the applied DC voltage. The dots are real data and the solid line is a theoretical fit according to the first order correction to the resonance frequency as stated in the body of the paper. A fit to the (0,1) resonance frequency shift using Eq. 2 yields a separation distance of 170 μm. The (0,2) mode experiences a smaller frequency shift because this mode has a stiffer mechanical spring constant.

filter. Measurements for the shifts in the mechanical resonance in Fig. 3 were performed only on cavity A. The acoustic frequency shifts displayed in Fig. 3 show different responses for two of the modes. As expected, the fundamental mode displays a larger frequency shift for the DC driving voltage because of the lower mechanical stiffness.

We typically find the resonance of the SRF cavity by using a pulse-ringdown technique.[40] The transmission signal is amplified coming out of the dilution refrigerator and passes through a Schottky diode detector to a sourcemeter. Referring the reader to Fig. 4, we observed a SRF resonance shift of about 35 kHz for cavity A, slightly over three linewidths while cavity B displayed about 25 kHz, or six linewidths, of frequency translation. In addition, the measured frequency-pull parameter of our cavities is $G \equiv (d\omega/dL) = 2\pi \cdot 3.2 \times 10^{10}$ Hz/m. The colorbar depicts 250 V as the maximum DC driving voltage, but it should be noted that the furthest resonance shift for cavity A was performed at 255 V. The full range of tunable bandwidth is slightly different between the two cavities due to small cavity geometric variations, machining imprecision, and the use of different membranes.

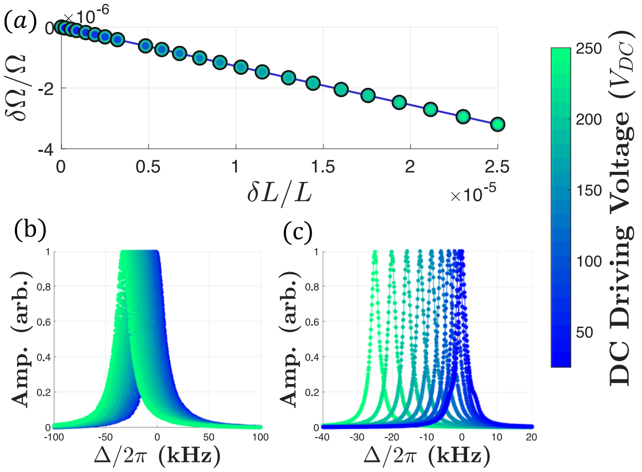

FIG. 4. (a) The fractional frequency shift of both SRF cavities at 10.3 GHz as a function of the fractional increase in cavity length at a temperature of T = 65 mK. The length change is determined from the standard equation for the TE_{011} mode and fitted, displayed as a solid line. (b), (c) Cavities A and B, respectively, normalized response plotted as a function of detuning Δ. Cavity A has loaded $Q_L = 1.1 \times 10^6$ while cavity B has a loaded $Q_L = 2.5 \times 10^6$.

Upon cooling down the fridge, there is negligible frequency shift of the cavities' resonance, aside from the superconducting transition, over the course of a week. There is no observable heat generated in the tuning process when we monitored the base fridge temperature.

V. CONCLUSION AND NEXT STEPS

We have demonstrated non-contact, non-invasive frequency tuning of a cm-scale superconducting radio frequency cavity. A great advantage of this technique is its potential for use with arbitrarily large high-Q cavities because the mechanism for tuning is external to the cavity. Moreover this mechanism for tuning avoids any potential heating challenges often found in piezoelectric devices. Future solid-body cylindrical cavities incorporating a membrane will have only one seam and display higher-Q cavities capable of similar frequency tuning. We anticipate this system will impact future work on 3D macroscopic cavity optomechanics.

For existing cavities with niobium end caps we aim to increase the Q by adding a curved end cap rather than the flat sections we used for these experiments. The membrane can also contribute to Q degradation because there exists a slight tip/tilt in the membrane with respect to the cavity axis that displaces the TE_{011} mode towards the boundary. As a result this can lead to reduced electrical contact between the two boundaries. These mechanisms lead to resistive losses in the surface current density and ultimately limit the achievable quality factor. Furthermore, future experiments seeking to incorporate a macroscopic membrane and maintain high-Q niobium cavities must investigate treatment options for the thin films. For example, while baking does generally improve the cavity Q, we are unable to bake the thin-film membrane in the same manner. Since the membrane constitutes almost 17% of the surface area of the cavity, this can lead to substantial losses.

For this cavity configuration the full bandwidth of tunable range has the potential to be greatly enhanced by examining Eq. 2. For example, the cubic dependence on the distance can be reduced from 170 μm that was used in this paper, the driving voltage can be increased further by using higher voltage-rated capacitors, and the mechanical spring constant can be lowered by incorporating lower stress membranes. One final improvement is to consider a different geometry in which one constructs a superconducting cavity with a central tuning post for larger bandwidth.[31]

ACKNOWLEDGMENTS

J.P. would like to thank Dr. K.C. Schwab for his advice and engaging discussions regarding the direction of the project. J.P. would also like to thank Sierra Amps, LLC for their direction and guidance with low-noise circuit design. The authors acknowledge support from DARPA through grant W911NF1510557.

[1] V. Arbet-Engels, C. Benvenuti, S. Calatroni, P. Darriulat, M. Peck, A.-M. Valente, and C. Van't Hof, Nuclear Instruments and Methods in Physics Research Section A: Accelerators, Spectrometers, Detectors and Associated Equipment **463**, 1 (2001).
[2] S. Kuhr, S. Gleyzes, C. Guerlin, J. Bernu, U. B. Hoff, S. Deléglise, S. Osnaghi, M. Brune, J.-M. Raimond, S. Haroche *et al.*, Applied Physics Letters **90**, 164101 (2007).
[3] A. Romanenko, A. Grassellino, O. Melnychuk, and D. Sergatskov, Journal of Applied Physics **115**, 184903 (2014).
[4] A. Romanenko, A. Grassellino, A. Crawford, D. Sergatskov, and O. Melnychuk, Applied Physics Letters **105**, 234103 (2014).
[5] M. Reagor, W. Pfaff, C. Axline, R. W. Heeres, N. Ofek, K. Sliwa, E. Holland, C. Wang, J. Blumoff, K. Chou *et al.*, Physical Review B **94**, 014506 (2016).
[6] R. W. Andrews, R. W. Peterson, T. P. Purdy, K. Cicak, R. W. Simmonds, C. A. Regal, and K. W. Lehnert, Nature Physics **10**, 321 (2014).
[7] X. Gu, A. F. Kockum, A. Miranowicz, Y.-x. Liu, and F. Nori, Physics Reports (2017).
[8] H. Rokhsari, T. Kippenberg, T. Carmon, and K. Vahala, IEEE Journal of Selected Topics in Quantum Electronics **12**, 96 (2006).
[9] L. Tóth, N. Bernier, A. Feofanov, and T. Kippenberg, Physics Letters A (2017).
[10] M.-A. Miri and A. Alù, JOSA B **34**, D68 (2017).
[11] C. Bekker, R. Kalra, C. Baker, and W. P. Bowen, Optica **4**, 1196 (2017).
[12] D. Lee, M. Underwood, D. Mason, A. Shkarin, S. Hoch, and J. Harris, Nature Communications **6**, 6232 (2015).
[13] P. A. Truitt, J. B. Hertzberg, C. Huang, K. L. Ekinci, and K. C. Schwab, Nano Letters **7**, 120 (2007).
[14] L. De Lorenzo and K. Schwab, New Journal of Physics **16**, 113020 (2014).
[15] H. Paik, D. Schuster, L. S. Bishop, G. Kirchmair, G. Catelani, A. Sears, B. Johnson, M. Reagor, L. Frunzio, L. Glazman *et al.*, Physical Review Letters **107**, 240501 (2011).

[16] A. Noguchi, R. Yamazaki, M. Ataka, H. Fujita, Y. Tabuchi, T. Ishikawa, K. Usami, and Y. Nakamura, arXiv preprint arXiv:1602.01554 (2016).

[17] M. Yuan, V. Singh, Y. M. Blanter, and G. A. Steele, Nature Communications **6**, 8491 (2015).

[18] M. Yuan, M. A. Cohen, and G. A. Steele, Applied Physics Letters **107**, 263501 (2015).

[19] C. Reece, P. Reiner, and A. Melissinos, Nuclear Instruments and Methods in Physics Research Section A: Accelerators, Spectrometers, Detectors and Associated Equipment **245**, 299 (1986).

[20] V. Ilchenko, P. Volikov, V. Velichansky, F. Treussart, V. Lefevre-Seguin, J.-M. Raimond, and S. Haroche, Optics Communications **145**, 86 (1998).

[21] F. Souris, H. Christiani, and J. Davis, Applied Physics Letters **111**, 172601 (2017).

[22] M. A. Cohen, M. Yuan, B. W. de Jong, E. Beukers, S. J. Bosman, and G. A. Steele, Applied Physics Letters **110**, 172601 (2017).

[23] L. A. Martinez, A. R. Castelli, W. Delmas, J. E. Sharping, and R. Chiao, New Journal of Physics **18**, 113015 (2016).

[24] M. Aspelmeyer, T. J. Kippenberg, and F. Marquardt, Reviews of Modern Physics **86**, 1391 (2014).

[25] A. Schliesser, P. Del'Haye, N. Nooshi, K. Vahala, and T. Kippenberg, Physical Review Letters **97**, 243905 (2006).

[26] A. Schliesser, R. Rivière, G. Anetsberger, O. Arcizet, and T. J. Kippenberg, Nature Physics **4**, 415 (2008).

[27] J. Teufel, T. Donner, D. Li, J. Harlow, M. Allman, K. Cicak, A. Sirois, J. D. Whittaker, K. Lehnert, and R. W. Simmonds, Nature **475**, 359 (2011).

[28] R. Kalra, A. Laucht, J. P. Dehollain, D. Bar, S. Freer, S. Simmons, J. T. Muhonen, and A. Morello, Review of Scientific Instruments **87**, 073905 (2016).

[29] E. Mykkänen, J. Lehtinen, A. Kemppinen, C. Krause, D. Drung, J. Nissilä, and A. Manninen, Review of Scientific Instruments **87**, 105111 (2016).

[30] A. AkkoÇ, *Design and Implementation of a Microwave Cavity Resonator for Modulated Backscattered Wave*, Ph.D. thesis, Middle East Technical University (2015).

[31] X. Liu, L. P. Katehi, W. J. Chappell, and D. Peroulis, Journal of Microelectromechanical Systems **19**, 774 (2010).

[32] N. C. Carvalho, Y. Fan, and M. Tobar, Review of Scientific Instruments **87**, 094702 (2016).

[33] M. H. Awida, D. Passarelli, P. Berrutti, I. Gonin, S. Kazakov, T. Khabiboulline, J. Holzabauer, T. Nicol, J. Ozelis, M. Parise *et al.*, IEEE Transactions on Nuclear Science **64**, 2450 (2017).

[34] J. Holzbauer, C. Contreras-Martinez, Y. Pischalnikov, W. Schappert, and J.-C. Yun, in *9th Int. Particle Accelerator Conf.(IPAC'18), Vancouver, BC, Canada, April 29-May 4, 2018* (JACOW Publishing, Geneva, Switzerland, 2018) pp. 2678–2680.

[35] J. Holzbauer, Y. Pischalnikov, W. Schappert, J.-C. Yun *et al.*, in Proc. LINAC (2016).

[36] M. Shoaib, N. Hisham, N. Basheer, and M. Tariq, Analog Integrated Circuits and Signal Processing **88**, 1 (2016).

[37] A. M. Elshurafa, K. Khirallah, H. H. Tawfik, A. Emira, A. K. A. Aziz, and S. M. Sedky, Journal of Microelectromechanical Systems **20**, 943 (2011).

[38] G. Ciovati, G. Myneni, F. Stevie, P. Maheshwari, and D. Griffis, Physical Review Special Topics-Accelerators and Beams **13**, 022002 (2010).

[39] S. Yanai, V. Singh, M. Yuan, M. Gely, S. Bosman, and G. Steele, Applied Physics Letters **110**, 083103 (2017).

[40] J. Knobloch, "Basic concepts of measurements made on superconducting rf cavities," Tech. Rep. (1991).

High-Q SRF 3D cavities for RF optomechanics

Jay E. Sharping* and Jacob Pate, Johnathon J. Thompson, Luis
A. Martinez, Alessandro R. Castelli, Jacob Parker, Raymond Chiao

(Dated: January 25, 2019)

In this paper we report on designs, simulations and experiments with two types of high-Q 3-dimensional cavities: cylindrical TE011, and coaxial quarter-wave stub. We investigate the dependence of Q on the practical implementation tolerances of gaps between components, shape imperfections, and frequency tunning strategies. We find that cylindrical cavities can maintain high Q for designs which include frequency tunability and mechanical oscillators as long as extraordinary care is taken with shape and gap tolerance during construction and assembly. Coaxial stub cavities can be made frequency tunable while maintaining high Q, but require more creativity to include a mechanical element. Finally, we report on a coaxial stub cavity incorporating a conically-shaped stub which confines the electric field near the stub's tip stub, thus enhancing field-matter interactions near the tip.

Usage: Secondary publications and information retrieval purposes.

PACS numbers: May be entered using the `\pacs{#1}` command.

I. BACKGROUND

The ability to use cavities to increase electromagnetic energy storage opens up the possibility of observing radiation interactions with matter[1, 2]. Specifically, radiation pressure acting on the boundaries or on other frequency-sensitive elements within the cavity gives rise to optomechanical phenomena such as parametric amplification, sideband cooling, and squeezing [3–11]. A large variety of cavity configurations for this purpose are possible, but superconducting radio-frequency (SRF) cavities[12, 13] are attractive because they can be constructed to confine high electric field strengths $E_{\max} \sim$ 10 MV/m while also maintaining high quality factors, $Q \sim 10^{10}$. The work of Schoelkopf, *et.al.,* [14–16] illustrates the value of such SRF cavities for fundamental studies of quantum mechanics. We propose, and are underway in, using these systems to observe quantum mechanical phenomena in cm-scale mechanical oscillators. The goal of this study is to provide a 3D macroscopic system capable of demonstrating parametric oscillation and amplification that leads to the Dynamical Casimir effect (DCE)[17–19].

In this paper we evaluate the effect that cavity imperfections have on Q for two cavity configurations: a cylindrical cavity (TE011 mode) and a quarter-wave ($\lambda/4$) stub cavity. In the $\lambda/4$ stub cavity we consider cylindrical and cone-shaped stubs. We pay attention to seams which might include resistive or electrically open interfaces between parts. We address shape imperfections (tilt and surface curvature) arising from machining tolerance limitations or etching effects, and geometric compressive distortions due to cavity fastening. We present simulation and experimental results for a frequency-tunable $\lambda/4$ stub cavity wherein we anticipate the ability to preserve the high Q. Finally, we indicate a preferred design strategy for subsequent SRF cavities for microwave optomechanical experiments.

Design constraints are extremely important considerations for achieving high Q in such systems[13, 20, 21]. It is straightforward to incorporate a mechanical element, such as a membrane, with a cylindrical SRF cavity, but adding components introduces lossy seams and dielectrics which can degrade the Q. On the other hand, it is not clear how to add mechanical transduction to the $\lambda/4$ SRF stub cavity.

II. SIMULATION DESIGN

Consider a single electromagnetic mode of interest within each of two types of cavities. In the cylindrical cavity (Fig. 1(a)-(c)) metallic walls enclose an empty cylinder which can support numerous transverse electric (TE) and transverse magnetic (TM) modes[22]. The TE011 mode, which is a donut-shaped mode, has a node in the magnetic and electric fields along the axis. The resonance associated with the TE011 mode exhibits a high Q owing to the fact that the fields are confined within the volume of the cavity, staying away from seams and boundaries. Note that the TM111 is frequency-degenerate with the TE011 mode, but the modes can be evaluated independently within the simulations. Experimentally we find that the degeneracy is typically lifted due to minor perturbations to the modes.

The second system we consider is a $\lambda/4$) stub cavity which is comprised of a coaxial waveguide section that is electrically-shorted on one end and electrically open on the other. The open part of the coaxial section connects to a cylindrical waveguide having a relatively high cutoff frequency[15]. There is evanescent decay of the fields within the cylindrical section which is made sufficiently long that very little energy leaks out the open end. The confined mode is a TEM-like field within the coaxial region, having a radially-directed electric-field and a mag-

---

* School of Natural Sciences, University of California Merced.

netic field which wraps around the axis. The shorted end creates a boundary condition where the electric field amplitude is zero, while there is an anti-node in the electric field amplitude near the end of the stub.

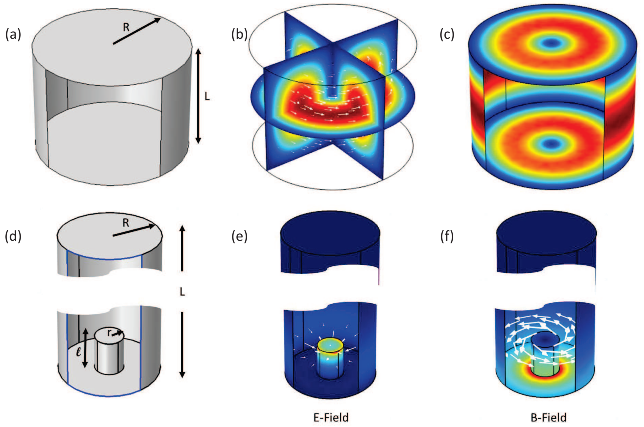

FIG. 1. Description of the cavities and modes used in this study.(a) - (c) illustrate the TE011 mode within a cylindrical cavity of radius R and height L. A simulation of the electric field is given in (b) where the "donut-shaped" mode is evident. The norm of the magnetic field at the surface is illustrated in (c) where we observe the relatively low field strength near the edges of the cylinder and maxima located at roughly 48% of the distance from the axis. (d) - (f) illustrate the $\lambda/4$ stub coaxial cavity. The electric field is plotted in (e) showing the TEM-like field extending radially towards the center. The electric field is largest at the rim of the cylindrical stub. (f) shows the magnetic field which encircles the axis of the system and has its maximum at the base of the stub.

TABLE I. Cavity parameters

$f = 10$ GHz	Resonance frequency
$R_s = 120$ nΩ	Surface resistance, $T = 40$ mK
Surface conductivities	
$\sigma_s = 1.0 \times 10^{-6}$ S/m	Air
$\sigma_s = 3.77 \times 10^{7}$ S/m	Normal metal
$\sigma_s = 1.0 \times 10^{14}$ S/m	Untreated Nb, $T = 40$ mK
$\sigma_s = 2.78 \times 10^{18}$ S/m	Fully treated Nb, $T = 40$ mK
Cylindrical cavity geometry	
$L = 30.07$ mm	Cylinder height
$R = 21.05$ mm	Cylinder radius
$G = 750$ Ω	Cylinder G-factor
Coaxial $\lambda/4$ cavity geometry	
$L = 55$ mm	Total height
$R = 7.0$ mm	Total height
$\ell = 5.0$ mm	Stub height
$r = 2.0$ mm	Stub radius
$G = 168$ Ω	$\lambda/4$ cavity G-factor

All finite element modeling is performed using COMSOL Multiphysics and RF Module software. The geometries (please see Table I) are created to give a resonance frequency of 10 GHz and to match those of prototypes in use within our laboratory. The materials in the simulations are chosen to be normal (non-superconducting) aluminum 6061, which is the material used in many of our prototypes, and air. Impedance boundary conditions are used for the boundary of the simulation, but special attention is given to be certain that all physical boundaries of the experimental system (such as air gaps in the pillbox and the open end in the coaxial stub) are properly accounted for. We then solve for eigenmodes in the desired frequency range and choose the mode of interest.

A. Eigenfrequency analysis - mode of interest

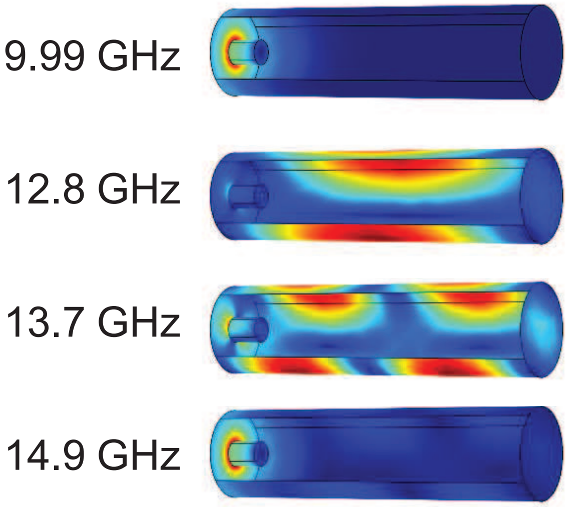

FIG. 2. Shown here are surface magnetic field plots for the four lowest frequency eigenmodes for a coaxial stub cavity. The lowest frequency eigenmode with the field confined near the stub is the mode of interest. The other modes will exhibit lower Q because energy can leak out the open end.

Using the modes of the $\lambda/4$ cavity as an example, Fig. 2 shows the surface magnetic field norm for four eigenmodes. The top one with a frequency of 9.99 GHz is the mode of interest. The field is mostly confined to the region of the stub and the field decays exponentially as a function distance from the tip of the stub in the cylindrical section. The other three modes, at higher frequencies, feature bound field profiles which do not evanescently decay in the cylindrical waveguide section.

In order to obtain high Q, the resonance frequency of the stub must be tuned away from the cutoff frequency of the cylindrical waveguide section and the cylindrical waveguide section must be long enough that the field decays by a factor of $\sqrt{Q}$. Figure 3 shows a semi-log plot of the electric field amplitude (normalized to the field amplitude at the tip of the stub) as a function of position along the axis of the structure. The field is negligible, as expected, within the metallic stub, becomes large at the surface of the stub, and then shows exponential decay from the tip of the stub towards the open end of the waveguide section. For the structure studied herein, the field is seen to decay by an amount greater than 10^{-6} over the length of the cylindrical waveguide section, and so we expect the Q due to waveguide leakage to be limited to $\sim 10^{12}$.

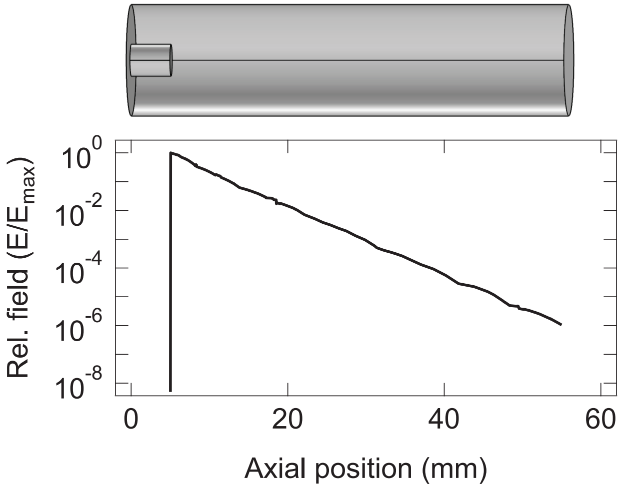

FIG. 3. The relative electric field amplitude as a function of axial position for a $\lambda/4$ stub cavity. If waveguide leakage is the only source of loss, Q is limited to $\sim 10^{12}$

B. Evaluation of G and Q

The dependence of Q on cavity design and material is captured in the relationship between cavity G-factor and the surface resistance, R_s. For cavities with uniform R_s, $Q = G/R_s$. The surface resistance, R_s, captures all surface-related resistive loss contributions and the cavity G-factor weights the field strength at the surface to that in the volume of the cavity according to:

$$G = \frac{\omega_0 \mu_0 \int\limits_V |H|^2 dv}{\int\limits_S |H|^2 ds}. \tag{1}$$

The G-factors for the geometrically perfect cylindrical cavity and the geometrically perfect $\lambda/4$ cavity are 750 Ω and 168 Ω, respectively. One can include all cavity loss mechanisms by modeling them as resistances and then evaluating the sum of resistive contributions from each mechanism. To use the open $\lambda/4$ cavity as an example, the loss through the open end can be included as a large surface resistance applied to the open boundary while superconducting surface resistance values can be applied to the superconducting walls. The values for G-factors imply that the cylindrical cavity should have more than 4-times the Q compared with the $\lambda/4$ cavity if the only losses are intrinsic material surface resistance losses in the cavity walls. We find, however, that the ability to fabricate a *seamless* $\lambda/4$ *cavity from a single piece of Niobium is critically important because* seams can introduce a dominant resistive loss contribution.

Cavity shape imperfections are seen as changes in the G-factor as well as changes in surface-related resistive losses. Such issues are included in the simulations by creating segments within the modeled geometry. For example, an air gap is included by replacing a segment of metallic wall with air. Resistive interfaces are modeled by replacing segments of superconducting metal having a high conductivity with normal metal having a lower conductivity. Shape imperfections are directly incorporated into the simulated cavity geometry. When imperfections, resistive seams or open gaps are present, we evaluate the quality factors by incorporating them into the simulation geometry and comparing the energy stored with the rate of energy lost in the cavity according to:

$$Q = \frac{\omega_0 \int\limits_V u_{\mathrm{tot}} dv}{\int\limits_S I_{\mathrm{loss}} ds}, \tag{2}$$

where u_{tot} is the energy density in the cavity, I_{loss} is the power lost, and ω_0 is the resonant frequency of the mode.

The accuracy of Eq. 2 depends on making reasonable simulation choices for the surface conductivity at each of the boundaries in the geometry. We calculate resistive losses for polished and heat treated niobium boundaries at 40 mK using a surface conductivity of $\sigma_s = 2.78 \times 10^{18}$ S/m. For niobium boundaries prior to polishing and heat treatment we use $\sigma_s = 1.0 \times 10^{14}$ S/m at 40 mK . For normal (non-superconducting) niobium boundaries we use $\sigma_s = 3.77 \times 10^7$ S/m. For air boundaries we use $\sigma_s = 1.0 \times 10^{-6}$ S/m. These quantities are used for all of our simulations and were determined by comparing simulation calculations with experimental measurements of Q for a $\lambda/4$ cavity under each of these conditions.

III. SIMULATION RESULTS

A. The cylindrical cavity

We simulate geometrically-perfect cavities to obtain benchmark values for $Q = 6.3 \times 10^9$ and $G = 750\Omega$. As shown in Fig. 1(a-c) the TE011 RF mode is confined within the volume of the cavity, therefore surface losses are minimized. In the case of the geometrically-perfect cylindrical cavity, Q is limited by surface resistance, $R_s = 120$ nΩ. For high purity Nb which has been etched and heat treated it is possible to obtain $R_s < 10$ nΩ[23, 24]. We select $R_s = 120$ nΩ because it is consistent with our experimental observations of etched and heat treated Nb cavities fabricated in our group. In experimental measurements on cylindrical cavities comprised of multiple parts, we have achieved $Q = 3 \times 10^8$.

Seams, *i.e.,* gaps where parts are fastened together, degrade the Q-factor and therefore are included in the simulation by adding a single cylindrical band near one end of the cavity. Fig. 4(a) shows simulated Q as a function of gap size ranging from 100 μm to 3 mm. The three curves represent a superconducting gap (control simulation), a gap comprised of normal metal, and an air gap. The Q decreases only slightly for gap sizes less than 250 μm regardless of whether they are metallic or air gaps. We estimate that standard machining and etching processes lead to gap sizes less than 100 μm. The reason for the small sensitivity to gap size for perfectly-shaped cylindrical cavities is that the mode is confined away from the location of the gap, so the denominator of Eq. 2 changes very little.

Shape imperfections, however, displace the mode towards cavity surfaces, and when combined with a gap lead to a degradation of Q for reasonable cavity fabrication tolerances. Figure 4(b) shows the degradation of Q as a function of parallelism of the end planes given by a tilt angle. In the simulation we choose a gap size of 100 μm and introduce a tilt between the top circular end plane and the axis of the system. The simulated gap is located near the bottom end plane whose normal is parallel with the cylinder axis. Here one observes a drop in Q for all cases as the tilt angle increases. The Q decreases slightly even for a superconducting gap because the G-factor decreases as a function of the field being displaced towards the surfaces. The reduction in Q is more pronounced when the gap is comprised of normal metal or air. Reasonable tolerances for parallelism indicate that we should expect tilt uncertainty as large as $1 - 10$ mRad which is seen to severely degrade the Q when combined with gaps. Heat plots of the surface magnetic field norm shown inset in Fig. 4(b) show that the field displaces towards the interface between the cylinder body and the end plane even when the tilt angle is an order of magnitude better than we expect to achieve. For a normal resistive gap the Q suffers by more than two orders of magnitude and is limited to 10^7. Note that this simulation overestimates the effect of the gap to some extent because the gap is uniformly large around the rim of the cylinder. One expects that the gap will make contact with the end plane in at least three places. In experiments where we use an indium superconducting metal gasket between components we routinely obtain $3 \times 10^7 < Q < 3 \times 10^8$.

In assembling a cylindrical cavity with dimensions on the order of a few centimeters from three components: two end planes and one cylindrical body, we can reasonably expect to obtain parallelism of ±3 mRad. Combined with ~ 100 μm gaps, we are limited to Q$\sim 10^7$. Clearly maintaining the tightest tolerances for gap size and parallelism are critical during fabrication.

This limit can be overcome to some extent by adding curvature to the ends of the cylinder. To evaluate this design choice we model *imperfect* cylindrical cavities having a slight curvature on the end walls. Figure 5(a) shows how, for a gap size of 100 μm and for various amounts of tilt, the Q improves as the end walls become more concave (*i.e.,* decreasing Rc). For example, we expect an increase in Q from 10^7 to 10^9 by introducing a radius of curvature of ~ 100 cm to both of the end planes. Figure 5(b) shows Q as a function of tilt angle for several radii of curvature. Reasonable machining tolerances indicate that curved end planes result in significant improvement in Q to values $\sim 10^9$.

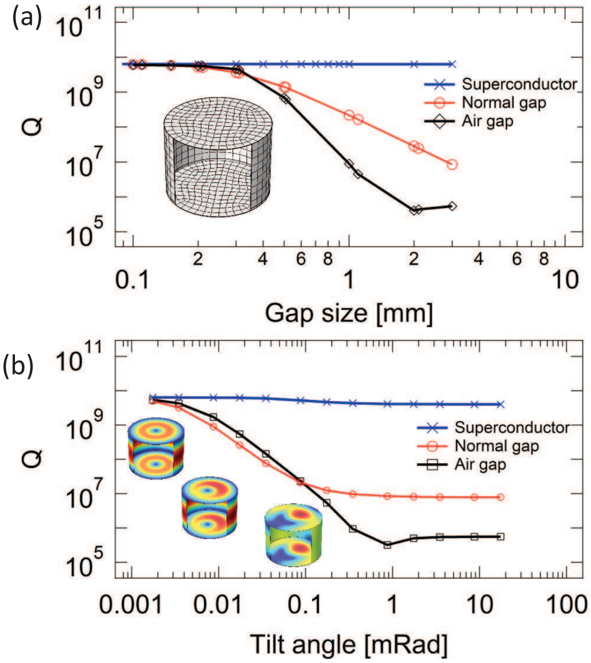

FIG. 4. Simulation results for a cylindrical cavity with a gap between the body and end of the cylinder. (a) shows the degradation of Q as a function of gap size for several equivalent gap materials. (b) shows the degradation of Q as a function of end-plane tilt angle for the case of a 100 μm gap. Note that Q degrades significantly when gaps and tilts are present in the system.

When using a cylindrical cavity as a sensor for end-plane motion it is essential to consider the surface quality of the elastic end plane separately from the rest of the cavity. For example, we aim to use Nb-coated silicon nitride membranes on one end of the cavity and to sense the motion of that membrane in response to external forces. In that case we will not be able to perform the same buffered chemical polish and heat treatment on the coated membranes as we can on the remainder of the cavity. If we sputter-coat silicon-nitride membranes we can use a model where the coated membrane takes on the conductive properties of *untreated* niobium. Considering the remainder of the cavity to suffer from 100μm gaps, 1 mRad tilt and a single curved end with a radius of curvature of 100 cm, the cavity Q is lowered from $Q = 6.9 \times 10^8$ to $Q = 1.8 \times 10^8$. Assuming a per-

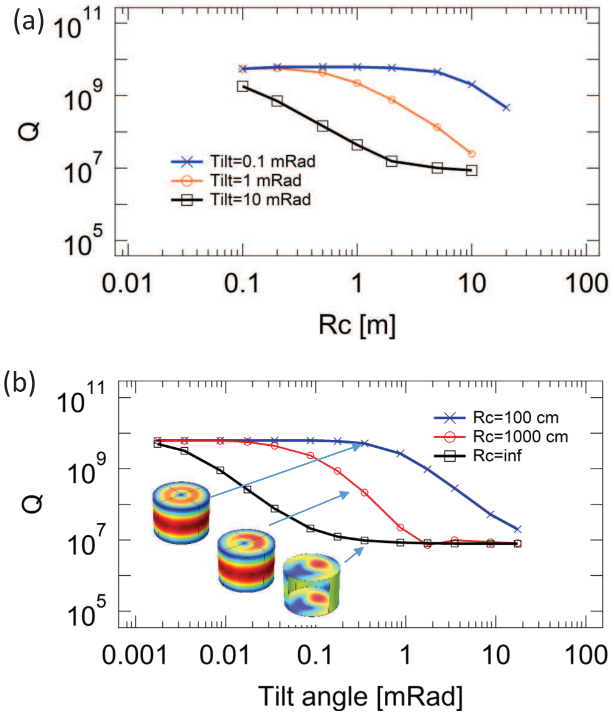

FIG. 5. Simulation results exploring the relationship between tilt angle, cavity end curvature, and Q. (a) shows Q as a function of radius of curvature for several different tilt angles. (b) shows Q as a function of tilt angle for several different radii of curvature. Note that tight fabrication tolerances suggest that Q$\sim 10^9$ is possible.

fectly aligned cavity without gaps the Q is lowered from $Q = 6.3 \times 10^9$ to $Q = 2.3 \times 10^8$. The quality factor is clearly limited by the surface resistance of the untreated boundary. Plasma deposition of Nb is an alternative to sputtering for the purpose of creating a film with low surface resistance.

B. The quarter-wave coaxial stub cavity

As mentioned earlier, for a given material surface resistance R_s, Eq. 1 combined with $Q = G/R_s$ allows us to calculate the expected cavity Q. The coaxial stub cavity with dimensions given in Table I has $G = 168\ \Omega$ which is somewhat lower than $G = 750\ \Omega$ for the cylindrical cavity. The reduction in G is due to the fact that the magnetic field is not as well confined within the cavity so the surface magnetic field is slightly larger than is the case for the cylindrical cavity. Moreover, there is no region on the surface where there is a null in the magnetic field, so any resistive seams that might be present will have a large effect on energy loss and reduce Q. Additionally, it is difficult to do high tolerance machining for such cavities because the tool must be longer than the length of the cylindrical section. For the designs considered here, the cylindrical section is 55 mm long and 14 mm in diameter. Since niobium is challenging to cut, it is challenging to fabricate anything other than a simple stub cavity. Using standard mill and lathe machines it is difficult to include supports for a membrane or other experimental element. The principal advantage of the coaxial stub cavity is that it features one open end and therefore *it can be fabricated from a single piece of metal.* There will not be seams unless the cavity is comprised of multiple parts fastened together. In this section we compare simulations of coaxial stub cavities which are geometrically perfect, cavities with hypothetical fabrication imperfections, and two-piece coaxial stub cavities. We include calculations for cylindrically-shaped and conically-shaped stubs.

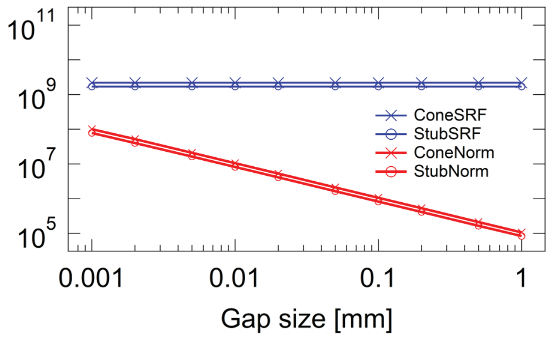

FIG. 6. Plots of Q as a function of gap size for coaxial $\lambda/4$ cavities. The results are cylindrical and conical stubs. The gap is located at the base of the outer wall of the cavity. The blue lines depict the case of a superconducting gap, which serves as a control simulation, while the red lines depict the response for a resistive gap with normal conductivity.

Figure 6 shows the variation in cavity Q as a function of gap size when a resistive gap is introduced at the interface between the outer cylinder and the bottom plane. The reduction in Q even for extremely small gaps of 1 μm is more than an order of magnitude owing to the fact that there is non-negligible surface magnetic fields in the region of the gap. This is seen in Fig. 7(b) where the light blue surface magnetic field is considerable along the entire bottom surface of the stub cavity. Assuming typical fabrication tolerances we expect that gaps will be larger than 1 μm, and so we will be limited to $Q < 10^7$. Note that we have simulated both the cylindrical stub and the conical stub where the conical stub has a slightly higher Q as a consequence of the reduction in the inside surface area of the cavity for that configuration.

Losses due to gaps at the base of the stub cavity dominate the Q in any imperfect cavity. The Q does not change significantly as a result of other geometrical imperfections such as stub tilt, axial offset, or cavity ellipticity.

It is the imperfections in the regions of high *magnetic field* which result in surface resistance losses in high-Q cavities. Therefore we have an opportunity to modify

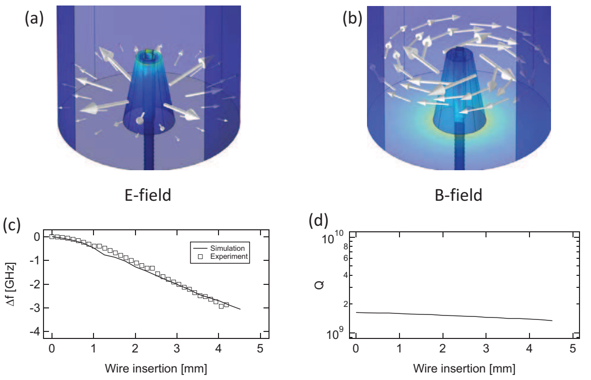

FIG. 7. Plots of the (a) electric and (b) magnetic field distributions in conical coaxial $\lambda/4$ stub cavities with an axial wire inserted for frequency tunability. Observe that the presence of the wire and hole at the tip of the stub do not significantly reduce Q because the magnetic field is small in that region of the cavity. (c) Simulation results and experimental data showing the frequency shift as a function of wire insertion. Once the wire insertion exceeds 1 mm, the frequency shifts linearly with a slope of 730 MHz/mm. (d) Plot of simulated Q as a function of insertion length showing that Q decreases only slightly with insertion.

the cavity in regions of low magnetic field, such as the top plane of the stub or at the tip of a conical stub. As an example, frequency tunability is achieved in a $\lambda/4$ cavity by adding a hole at the end of the stub along the cavity axis, and actuating a wire into the cavity along the axis. In this way the length of the stub is adjustable, which changes the resonant frequency.

Figure 7 shows the results of experiments and simulations of frequency tunability. From Fig. 7(a) and (b) we learn the nature of the electric and magnetic fields for the case of a wire inserted axially into the cavity. The mode does not vary significantly from that of the simple cone. The simulated and experimental frequency shifts are shown in Fig. 7(c). The experimental data is obtained using an aluminum cavity constructed as shown. The resonance is tracked using a network analyzer and the experiment is performed at room temperature. The agreement between the frequency shift expected according to the simulation and that realized experimentally is excellent. The important conclusion, graphically presented in Fig. 7(d) is that we expect to be able to construct frequency-tunable SRF cavities having $Q \sim 10^9$. The fact that structures can be introduced in this location of the cavity without significantly perturbing the Q of the cavity also suggests that we may be able to introduce a resonant structure which efficiently couples microwave and mechanical modes.

IV. DISCUSSION AND CONCLUSIONS

It is possible to construct high-Q ($\sim 10^9$) SRF cavities with resonances in the 10 GHz frequency range, and it is possible to include frequency tunability or other functional elements within the cavity. The principal challenges are: 1) using high quality niobium and careful processing to obtain a low surface resistance; 2) selecting cavity electromagnetic modes with a large G-factor, meaning that the ratio of the magnetic field strength in the volume of the cavity to that near the surface is maximized; 3) maintaining cavity symmetry during fabrication so that the magnetic field is not perturbed out towards the surface; and 4) eliminating seams or other resistive elements from regions of high magnetic field.

Cylindrical cavities are compared with coaxial $\lambda/4$ stub cavities. We find that the construction and assembly of multi-part cylindrical cavities is challenging because of the introduction of asymmetry in the cylindrical shape, and gaps where the parts fit together. Moreover, we find that the introduction of functionality in cylindrical cavities, such as a movable end wall for frequency tunability or mechanical coupling, or coupling to a second identical cavity is straightforward to do, but is generally accompanied by the introduction of even more gaps and asymmetry which can dramatically reduce the quality factor. Subsequently it requires much experimentation or unusually tight fabrication tolerances in the machining and polishing of the cavities in order to obtain $Q > 10^9$.

The coaxial $\lambda/4$ stub cavity is comparatively easy to make from a single piece of Nb, which simplifies the construction of a base cavity without seams. The inclusion of structures for frequency tunability or mechanical coupling is simplified by having access to the end of the stub, where the electric field is maximized but the magnetic field is minimized. In this way one can add functionality which couples to the electric field but which does not significantly reduce the Q of the cavity.

---

[1] G. Rempe, F. Schmidt-Kaler, and H. Walther. Observation of sub-poissonian photon statistics in a micromaser. *Physical Review Letters*, 64(23):2783, JUN 4 1990 1990. PT: J; TC: 444; UT: WOS:A1990DG88700014.

[2] D. Meschede, H. Walther, and G. Muller. One-atom maser. *Physical Review Letters*, 54(6):551–554, 1985 1985. PT: J; TC: 884; UT: WOS:A1985ABE0200017.

[3] Markus Aspelmeyer, Tobias J. Kippenberg, and Florian Marquard. Cavity optomechanics. *Reviews of Modern Physics*, 86(4):1391–1452, DEC 30 2014. PT: J; TC: 655; UT: WOS:000347201400001.

[4] Markus Aspelmeyer, Pierre Meystre, and Keith Schwab. Quantum optomechanics. *Physics Today*, 65(7):29–35, JUL 2012. PT: J; NR: 40; TC: 0; J9: PHYS TODAY; PG: 7; GA: 972TE; UT: WOS:000306302300018.

[5] E. Verhagen, S. Deleglise, S. Weis, A. Schliesser, and T. J. Kippenberg. Quantum-coherent coupling of a mechanical oscillator to an optical cavity mode. *Nature*,

482(7383), FEB 2 2012 2012. PT: J; TC: 21; UT: WOS:000299726000035.

[6] L. D. Tth, N. R. Bernier, A. K. Feofanov, and T. J. Kippenberg. A maser based on dynamical backaction on microwave light. *Physics Letters A*, Available online 30 May 2017 2017. ID: 271541.

[7] L. D. Toth, N. R. Bernier, A. Nunnenkamp, A. K. Feofanov, and T. J. Kippenberg. A dissipative quantum reservoir for microwave light using a mechanical oscillator. *Nature Physics*, 13(8):787–793, AUG 2017. PT: J; TC: 7; UT: WOS:000406778100019.

[8] R. A. Norte, J. P. Moura, and S. Groblacher. Mechanical resonators for quantum optomechanics experiments at room temperature. *Physical Review Letters*, 116(14):147202, APR 5 2016. PT: J; TC: 52; UT: WOS:000373587200004.

[9] R. W. Peterson, T. P. Purdy, N. S. Kampel, R. W. Andrews, P. L Yu, K. W. Lehnert, and C. A. Regal. Laser cooling of a micromechanical membrane to the quantum backaction limit. *Physical Review Letters*, 116(6):063601, FEB 8 2016. PT: J; TC: 45; UT: WOS:000369736200003.

[10] R. W. Andrews, R. W. Peterson, T. P. Purdy, K. Cicak, R. W. Simmonds, C. A. Regal, and K. W. Lehnert. Bidirectional and efficient conversion between microwave and optical light. *Nature Physics*, 10(4):321–326, APR 2014. PT: J; TC: 220; UT: WOS:000334068200021.

[11] J. D. Teufel, T. Donner, M. A. Castellanos-Beltran, J. W. Harlow, and K. W. Lehnert. Nanomechanical motion measured with an imprecision below that at the standard quantum limit. *Nature Nanotechnology*, 4(12):820–823, DEC 2009. PT: J; TC: 258; UT: WOS:000272415600013.

[12] Gianluigi Ciovati. Review of the frontier workshop and q-slope results. *Physica C-Superconductivity and its Applications*, 441:1, JUL 15 2006 2006. PT: J; CT: 12th International Workshop on RF Superconductivity; CY: JUL 10-15, 2005; CL: Cornell Univ, Ithaca, NY; TC: 8; UT: WOS:000238875600009.

[13] Charles E. Reece and Gianluigi Ciovati. Superconducting radio-frequency technology r&d for future accelerator applications. *Reviews of Accelerator Science and Technology, Vol 5: Applications of Superconducting Technology to Accelerators*, pages 285–312, 2012. PT: S; UT: WOS:000369837600012.

[14] Hanhee Paik, D. I. Schuster, Lev S. Bishop, G. Kirchmair, G. Catelani, A. P. Sears, B. R. Johnson, M. J. Reagor, L. Frunzio, L. I. Glazman, S. M. Girvin, M. H. Devoret, and R. J. Schoelkopf. Observation of high coherence in josephson junction qubits measured in a three-dimensional circuit qed architecture. *Phys.Rev.Lett.*, 107(24):240501, Dec 2011.

[15] Matthew Reagor, Wolfgang Pfaff, Christopher Axline, Reinier W. Heeres, Nissim Ofek, Katrina Sliwa, Eric Holland, Chen Wang, Jacob Blumoff, Kevin Chou, Michael J. Hatridge, Luigi Frunzio, Michel H. Devoret, Liang Jiang, and Robert J. Schoelkopf. Quantum memory with millisecond coherence in circuit qed. *Physical Review B*, 94(1):014506, JUL 8 2016. PT: J; UT: WOS:000379701200004.

[16] C. Axline, M. Reagor, R. Heeres, P. Reinhold, C. Wang, K. Shain, W. Pfaff, Y. Chu, L. Frunzio, and R. J. Schoelkopf. An architecture for integrating planar and 3d cqed devices. *Applied Physics Letters*, 109(4):042601, JUL 25 2016. PT: J; UT: WOS:000381688900031.

[17] P. D. Nation, J. R. Johansson, M. P. Blencowe, and F. Nori. Colloquium: Stimulating uncertainty: Amplifying the quantum vacuum with superconducting circuits. *Reviews of Modern Physics*, 84(1):1–24, Jan.-March 2012 2012. PT: J; UT: INSPEC:12587938.

[18] V. V. Dodonov. Current status of the dynamical casimir effect. *Physica Scripta*, 82(3):038105, SEP 2010. PT: J; UT: WOS:000281537200033.

[19] N. A. Inan, J. J. Thompson, and R. Y. Chiao. Interaction of gravitational waves with superconductors. *Fortschritte Der Physik-Progress of Physics*, 65(6-8):1600066, JUN 2017. PT: J; CT: Conference on Frontiers of Quantum and Mesoscopic Thermodynamics (FQMT); CY: JUL 27-AUG 01, 2015; CL: Prague, CZECH REPUBLIC; SI: SI; UT: WOS:000403351700031.

[20] C. E. Reece, P. J. Reiner, and A. C. Melissinos. Parametric converters for detection of small harmonic displacements. *Nuclear Instruments & Methods in Physics Research Section A-Accelerators Spectrometers Detectors and Associated Equipment*, 245(2-3):299–315, MAY 1 1986 1986. PT: J; TC: 15; UT: WOS:A1986C500100010.

[21] Matthew Reagor, Hanhee Paik, Gianluigi Catelani, Luyan Sun, Christopher Axline, Eric Holland, Ioan M. Pop, Nicholas A. Masluk, Teresa Brecht, Luigi Frunzio, Michel H. Devoret, Leonid Glazman, and Robert J. Schoelkopf. Reaching 10 ms single photon lifetimes for superconducting aluminum cavities. *Applied Physics Letters*, 102(19):192604, MAY 13 2013 2013. PT: J; TC: 7; UT: WOS:000320440800067.

[22] David M. Pozar. *Microwave engineering*. Fourth edition. Hoboken, NJ : Wiley, 2012] 2012,] 2012. Includes bibliographical references and index.; ID: 9910153599402121.

[23] G. Ciovati, G. Myneni, F. Stevie, P. Maheshwari, and D. Griffis. High field q slope and the baking effect: Review of recent experimental results and new data on nb heat treatments. *Physical Review Special Topics-Accelerators and Beams*, 13(2):022002, FEB 2010. PT: J; UT: WOS:000275059100008.

[24] Anne-Marie Valente-Feliciano. Superconducting rf materials other than bulk niobium: a review. *Superconductor Science & Technology*, 29(11):113002, NOV 2016. PT: J; TC: 3; UT: WOS:000385424400001.

A parametric oscillator for classroom demonstration or student laboratory

Alison Huff, Johnathon Thompson, Jacob Pate, Raymond Chiao, and Jay E. Sharping

School of Natural Sciences, University of California-Merced, 5200 Lake Road,
Merced, CA 95343 USA

E-mail: `jsharping@ucmerced.edu`

Abstract. We describe a simple and intuitive parametric oscillator apparatus which is suitable for a classroom demonstration or an upper division laboratory. In order to facilitate the incorporation of this apparatus into the physics curriculum, we provide the learning objectives for an upper-division physics laboratory experiment. We present typical experimental data illustrating the main features of parametric oscillators including oscillation threshold, frequency shifting at large amplitude and bistability. Our experiments and theory emphasize identifying the lowest-order threshold for oscillation in terms of the modulation depth and quality factor. This experiment provides a foundation for understanding current research such as that in quantum opto-mechanics and nonlinear dynamics.

1. Introduction

The pendulum is a powerful tool for teaching physics [1]. Give it a shove and it swings back and forth, and such direct excitation of an underdamped pendulum is part of the standard course in mechanics [2]. It turns out, however, that one can excite a pendulum's motion by varying a *parameter* such as the length or effective acceleration due to gravity. A classical analysis is sufficient to understand the behavior of a parametrically-excited simple pendulum but parametric amplification and oscillation are integral to modern experimental quantum physics [4–7]. These so-called parametric processes actually amplify the existing motion of the pendulum such that, assuming the effective *parametric gain* is greater than dissipative losses, the pendulum's motion will grow to a large amplitude. The existing oscillator motion is usually classical in its origin but the harmonic oscillator in its quantum ground state still exhibits zero-point fluctuations (quantum noise) and parametric excitation amplifies those fluctuations [3].

In this paper we describe an experimental parametric oscillator demonstration for use in the undergraduate college physics or mathematics curriculum. We describe a simple pendulum whose length is varied sinusoidally using a rotational servo-motor (see Fig. 1). We analyze the motion of the pendulum as recorded using a video camera or a photo sensor and characterize the system as a function of modulation depth and frequency. We present data and theory for the threshold of oscillation ($h > 2/3Q$) and experimentally map out the transient behavior as the system converges to a steady state. Finally, we present bistabilty curves as an example of the nonlinear dynamics observable using this apparatus.

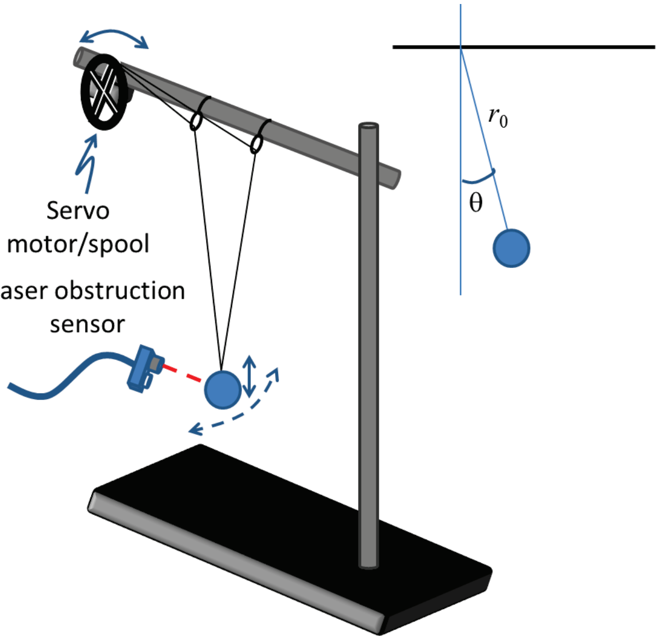

Figure 1. Schematic of the parametrically-driven pendulum. The motion of the servo motor results in a variation in the length of the pendulum as a function of time. The quantities r_0 and θ are given as shown in the inset.

The use of parametric oscillators in classrooms and teaching laboratories is not new. Lars Falk [8] created a set of experiments connecting the mathematics and physics of parametric oscillations. The three experiments: “the spring pendulum”, “parametric waves on a string”, and “parametric circuit oscillations” each allowed the student to obtain predictable and quantitative results. William Case analyzed a coupled pendulum system where the oscillator is attached to a platform suspended from above by springs [9]. By arranging for the platform resonant frequency to be twice that of the pendulum, one can set the platform in motion and observe the parametric excitation of motion of the pendulum.

The Mathieu equation ($\ddot{\theta} + \omega_0^2\left[1 + Fsin(\omega_e t)\right]\theta = 0$) describes many parametric resonance experiments including the simple pendulum with an oscillating support [8,9]. In the standard equation of motion for a simple pendulum the oscillating support is included as a time-dependent addition to the acceleration due to gravity. Case et al., [10] also analyzed the motion of a seated child on a swing revealing the combined linear and parametric excitation of the swing. One attractive feature of parametric oscillators is that nonlinear dynamics is readily observed. Berthet, et al., [11] devised an electronic parametric oscillator (an analog and digital circuit) which shows subcritical and supercritical bifurcations as a function of experimentally accessible variables. Curzon, et al., [12] constructed a *plus-shaped* oscillator using hollow tubes wherein a rod with plug is moved pneumatically within the vertical tube to achieve the parametric excitation. The system constructed in this way (in the absence of damping) is also described by a Mathieu-like equation, except that the periodic parametric excitation is a square wave rather than a sinusoid. A strength of Curzon's demonstration is that the resonant frequency is low enough (roughly 0.2 Hz) to visually observe changes in the behavior of the pendulum in real time. Eugene Butikov [13] presents analysis and computer simulation of a torsion spring oscillator wherein the moment of inertia of the rotor is parametrically modulated. Again, this system is described mathematically by the Mathieu equation. In his own words "This physical system, being useless for any practical application, is nevertheless ideal for gaining conceptual knowledge about the basics of parametric resonance..."

In contrast to the schemes described above, our experiment consists of a pendulum on a *fixed support* but with a time-varying *length.* It is no longer described by a Mathieu equation. The time-dependent length results in a time-dependent moment of inertia which enters into the equation of motion for the pendulum differently. In the standard form, the equation of motion now has time-dependent coefficients of the position and velocity (see Eq. 4). An excellent theoretical and numerical analysis of the problem is given by Belyakov, et al., [14, 15].

Our work provides an experimental system to be used alongside the analysis of Ref. [14, 15], which theoretically analyzed a pendulum having a periodically driven length. We are not aware of another classroom demonstration of the pendulum of varying length. The use of an open-source micro-controller adds unprecedented flexibility in determining the driving frequency (or frequencies) and parameter modulation depth, while also enabling automated data acquisition of the position and/or velocity of the pendulum as a function of time. In sum, our demonstration combines intuitive and quantitative understanding in an inexpensive and simple system.

2. Undergraduate laboratory objectives and typical experimental results

Consider an undergraduate experiment where the objectives are to: 1) experimentally observe and quantify damped harmonic motion of a pendulum; 2) derive the threshold conditions for the lowest and next-lowest order parametric oscillations; 3) predict the modulation depth required to induce parametric oscillations; and 4) experimentally observe and quantify the parametrically-driven pendulum motion. As learning outcomes, students will demonstrate: 1) the ability to assemble and debug a simple, weakly-damped, pendulum having a single mode of oscillation and identify the likely key sources of dissipation; 2) the ability to record and extract relevant data from video or sensors, and integrate the computer-controlled servo motor; 3) the ability to use Newtonian and/or Lagrangian mechanics to derive equations of motion and to manipulate those equations into forms that predict or explain observed experimental behavior; 4) the ability to generate and interpret plots of experimental data in both the time domain and frequency domain allowing them to extract key features of the oscillator such as dissipation or gain, resonance frequency, and quality factor (Q); and 5) explain the difference between a standard driven pendulum and a parametrically driven pendulum, explain the concept of a threshold of oscillation, and enumerate the conditions for parametric oscillation above threshold.

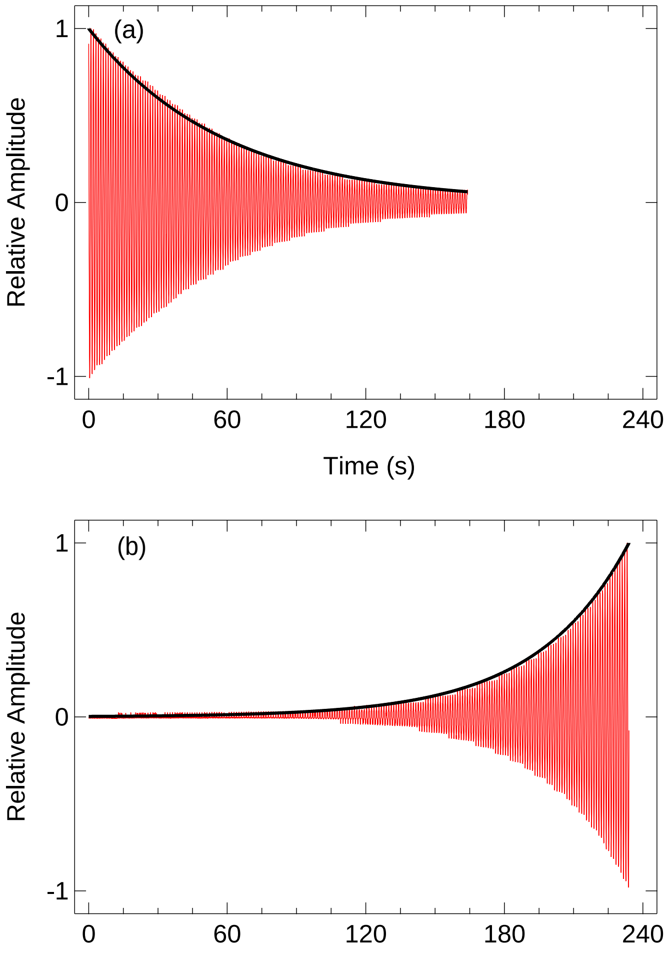

Figure 2. (a) Relative amplitude of an *undriven* pendulum as a function of time (red thin lines). The plot shows the ringdown in the damped harmonic motion. The damping parameter $\gamma = 0.017\ \mathrm{s}^{-1}$ is obtained by fitting a curve to the slowly varying envelope (heavy black line) of the oscillations ($Q = 173 \pm 3$). (b) Relative amplitude as a function of time for the same oscillator subject to a time-dependent length r_0, *i.e.,* parametric excitation (red thin lines). The exponential slowly-varying envelope, showing net gain in the energy of the pendulum, is plotted as a heavy black line.

The laboratory setup used throughout this paper is depicted in Fig. 1. A drilled wooden ball and nylon cord from Arbor Scientific's "drilled physics ball set" are used for the pendulum. The wooden ball having a diameter of 2.56 ± 0.01 cm is suspended in a

"V" configuration so that motion is constrained to a plane. We use a homemade wooden stand to suspend the pendulum, but a standard laboratory stand would be ideal. The length of the pendulum is varied by threading the pendulum's strings through eyelets and attaching them around a spool fastened to a rotational servo motor whose position is varied sinusoidally as a function of time using an Arduino microcontroller (Uno). The servo motor (SpringRC SM-S2309S - Micro Analog Servo) and spool combination are oriented so that, as they rotate, they pull the strings in a direction parallel with the axis of the horizontal supporting rod and smoothly move the bob up and down. By wrapping the string around the spool one obtains a linear dynamic range of modulation which exceeds the diameter of the ball. The frequency and angular amplitude of servo rotation are user defined. The corresponding modulation depth, $h = \frac{\delta r}{r_0}$, is calibrated experimentally. We record data in one of two ways. First, a digital camera (Cannon PowerShot) is used to record videos (in .avi format) of the motion of the pendulum against a black backdrop. The data, angular position as a function of time, is extracted from movies of the pendulum using a MATLAB program (available from the author on request) which loads each frame sequentially, locates the position of the center of the bob and records its position. As an example, for an undriven pendulum, an experimental measurement of relative amplitude as a function of time for a pendulum whose length is $r_0 = 28.5 \pm 0.5$ cm, is shown in Fig. 2. The exponential decay curve is highlighted where the damping parameter is found to be $\gamma = 0.017$ s^{-1} and the frequency is $f_0 = \frac{\omega_0}{2\pi} = 0.93 \pm 0.01$ Hz. The second technique employs a laser obstruction sensor (Waveshare Laser Receiver Module Laser Sensor Module) which produces a binary signal indicating the obstruction of the beam by the pendulum bob. The microcontroller is programmed to calculate the passage time as the pendulum swings which can then be used to calculate the energy stored in the oscillating pendulum. Passage time as a function of time are saved using an SD shield (HiLetgo Mini Logging Recorder Data Logger Module Shield V1.0) and SD memory card. Note that the servo motor, laser sensor and logger are all integrated on a single microcontroller. Programs are available through the Arduino users forum or upon request from the author.

Typical data for a parametrically-driven pendulum are given in Fig. 2(b). It is critical to note that to observe the lowest order parametric oscillations the driving frequency (1.88 Hz in this case) is twice the characteristic resonance frequency of the pendulum. The modulation depth must be large enough to exceed the threshold. For the data in Fig. 2(b), $h = \frac{\delta r}{r_0} = 0.014$ is 3-times larger than the threshold value predicted by $h = 2/3Q = 0.004$. The exponential amplitude gain coefficient is obtained by an experimental comparison with the data in Fig/2(b)and is $\mu = 0.025$ s^{-1} according to $A = A_0 e^{\mu t}$.

3. Threshold of a parametric oscillator

For a parametric oscillator, mechanical or otherwise, the modulation depth required to exceed the threshold for sustained oscillations is a key quantity. To obtain the threshold from first principles, we begin by considering the equation of motion and general solution for a weakly-damped, γ, pendulum of length, r_0, and small displacement angle, θ:

$$\ddot{\theta} + 2\gamma\dot{\theta} + \omega_0^2\theta = 0 \tag{1}$$

$$\theta(t) = Ae^{-\gamma t}\sin(\omega_0 t) + Be^{-\gamma t}\cos(\omega_0 t) \tag{2}$$

where $\omega_0 = \sqrt{\frac{g}{r_0}}$ is the natural resonance frequency of the pendulum and g is the acceleration due to gravity. The solutions are harmonic oscillations with a decaying exponential envelope. The case of parametrically driving the simple pendulum by varying its length requires further analysis. One can devise an equation of motion for the pendulum for small angular displacement in terms of the pendulum length, r, and angular position, θ. We must include a time-dependent radius and a damping term. The radius is given by:

$$r\left(t\right) = r_0\left(1 + h\sin\left(2\omega_0 t\right)\right) \tag{3}$$

where $h = \frac{\delta r}{r_0}$ is a modulation depth. Damping is added as an angular-velocity-dependent term to give a new equation of motion

$$\ddot{\theta} + 2\frac{\dot{r}\left(t\right)}{r\left(t\right)}\dot{\theta} + 2\gamma\dot{\theta} + \frac{g}{r\left(t\right)}\theta = 0, \tag{4}$$

wherein we see that a damping coefficient γ is included in the standard form of a damped simple harmonic oscillator (see Eq. (1)). We will look for solutions of the form

$$\theta\left(t\right) = a\left(t\right)\sin\left(\omega_0 t\right) + b\left(t\right)\cos\left(\omega_0 t\right), \tag{5}$$

where

$$\begin{aligned} a\left(t\right) &\propto e^{\mu t} \\ b\left(t\right) &\propto e^{\mu t}, \end{aligned} \tag{6}$$

represent slowly varying envelope functions. Note that if the parametric driving is absent, Eq. (4) reduces to Eq. (1) and $\mu \to -\gamma$ so that the solution is given by Eq. (2) where the oscillations are gradually attenuated. When parametric driving is present we will search for conditions of amplification, where $\mu > 0$ and real.

We obtain a system of two equations for $a(t)$ and $b(t)$ by inserting Eqs. (3), (5), and (6) into Eq. (4), and collecting coefficients of $\sin(\omega_0 t)$ and $\cos(\omega_0 t)$. We then discard second derivatives, which are small relative to the first derivatives and will not affect the threshold. The resulting coefficient for cosine is

$$\left(a(t)\left(\frac{3}{2}h\omega_0^2 + 2\mu\omega_0 + 2\gamma\omega_0 + \gamma\mu h\right) + b(t)\left(2\gamma\mu + 2h\mu\omega_0 - h\mu\omega_0 - h\gamma\omega_0\right)\right) = 0, \tag{7}$$

while for sine is

$$\left(a(t)\left(2\gamma\mu - 2h\mu\omega_0 + h\mu\omega_0 + h\gamma\omega_0\right) + b(t)\left(\frac{3}{2}h\omega_0^2 - 2\mu\omega_0 - 2\gamma\omega_0 + \gamma\mu h\right)\right) = 0. \tag{8}$$

The terms multiplying cosine and sine must be independently zero. For the purposes of establishing a threshold of oscillation, we seek out the terms of Eq. (7) and Eq. (8) only up to first order in h. With only these terms written in matrix form we have

$$\begin{bmatrix} \frac{3}{2}h\omega_0^2 + 2\mu\omega_0 + 2\gamma\omega_0 & 2\gamma\mu \\ 2\gamma\mu & \frac{3}{2}h\omega_0^2 - 2\mu\omega_0 - 2\gamma\omega_0 \end{bmatrix} \begin{bmatrix} a(t) \\ b(t) \end{bmatrix} \tag{9}$$

Upon evaluating the determinant of the left-most matrix and setting it equal to zero, we identify the conditions when this system gives a positive value for μ, which is the condition for exponential growth in the amplitude of the oscillations. The threshold is given by

$$h \geq \frac{4\gamma}{3\omega_0} = \frac{2}{3Q}. \tag{10}$$

Note that $h = \frac{\delta r}{r_0}$ is an amplitude modulation depth.

Equation 10 is a key result in this investigation. The quality factor, Q, on the right-hand side is critical as it captures many physical concepts associated with the oscillator [**?**]. There are three common ways of understanding Q. Firstly, the reciprocal of the *sharpness* of the resonance peak in a plot of energy as a function of driving frequency is given by $Q = \frac{\omega_0}{2\gamma}$. A large Q corresponds to a narrow resonance. Secondly, we can relate Q to the number of oscillations occuring over the decay time, $Q = \pi\frac{\text{decay time}}{\text{period}}$. A large Q indicates that the oscillator *rings* for a long time. Thirdly, the quality factor reflects the ratio of energy stored to that dissipated during a single cycle, $Q = 2\pi\frac{\text{energy stored}}{\text{energy dissipated}}$. A large Q means that the oscillator can store a large amount of energy. For our pendulum, $Q = 173 \pm 3$.

The third discussion of the quality factor, the one relating energy stored to that dissipated, gives us a physical basis under which we can also understand the meaning of the threshold condition. Equation 10 tells us that in order to achieve a net gain we must do enough work on the system by modulating the parameter, h, that we overcome the dissipation in the system.

4. Oscillation threshold data

We show experimental data describing temporal behavior of the parametric oscillator in Fig. 3 where we plot the steady-state energy in a 27.4 ± 0.5-cm long pendulum as a function of time for five different modulation depths. The time origin is determined by the onset of measurable oscillation. As expected, the ring-up time is shorter and the steady-state energy is larger as the modulation depth increases. For the case of larger modulation depths, we also observe transient oscillations which die out as the system reaches steady-state.

We study the oscillation threshold and frequency response by observing the steady-state energy of as a function of modulation depth and modulation frequency, respectively. The response of the system as a function of frequency is plotted in Fig. 4(a) for the case of a modulation depth of $h = \frac{\delta r}{r_0} = 0.031$, which is well above the threshold for

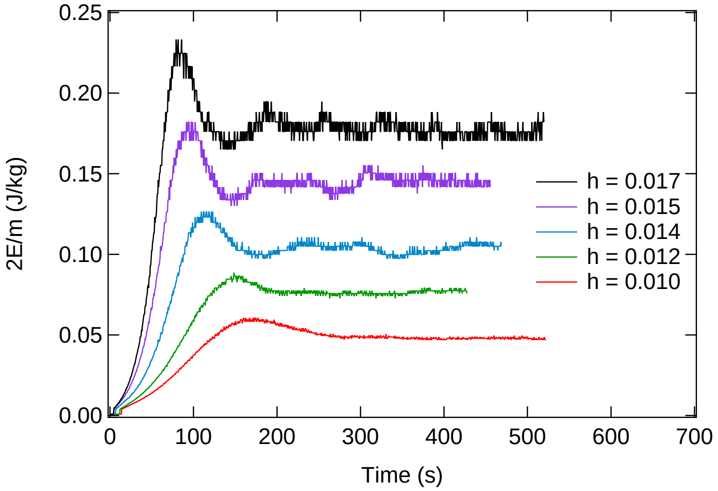

Figure 3. Plot of oscillator energy ($2E/m$) as a function of time for five different modulation depths. Larger modulation depths produce a rapid ring-up time and result in higher steady-state energies after transient variations dissipate.

the lowest order resonance. The peak in energy is not located at the second-harmonic driving frequency of $f = 2f_0 = 1.90 \pm 0.02$ Hz. Rather it is shifted to a lower value of 1.86 Hz. This is a consequence of the large angular amplitude of oscillation obtained and the need to relax the small-angle approximation which linearizes the simple pendulum. Due to the nonlinearity of the system, we expect that the resonance frequency of a pendulum will decrease by as much as 10% for the largest amplitudes observed here [**?**]. The observed shift in modulation frequency shown in Fig.4(a) is less than that expected for nonlinear oscillations because the pendulum's motion is initially linear as it is seeded by random noise.

The threshold behavior for modulation near the resonant condition is plotted in Fig. 4(b). Experimentally, for modulation depths less than $h = 0.0085$ the pendulum is not excited, and the energy remains zero; when we perform a linear fit to the 5 data points just above threshold, we see that the extrapolation yields a zero-crossing of $h = 0.0075 \pm 0.0005$. The energy increases gradually when the modulation depth increases beyond the threshold. The energy continues to increase as a function of modulation depth, which reflects the fact that the parametric amplification per cycle increases, but it is important to note that the case of energy greater than ~ 0.1 J/kg already already exceeds the point at which the pendulum can be considered "linear". The experimentally-obtained value for the threshold modulation depth ($h_{\text{exp}} = 0.0075 \pm 0.0005$) is nearly double the theoretically expected value given in Eq. (10) as $h_{\text{theory}} = \frac{\delta r}{r_0} = 0.0038 \pm 0.0003$, which assumes our experimentally measured value for dissipation ($\gamma = 0.017$ s^{-1}, and $Q = 173 \pm 3$) from the data in Fig. 2(a). The discrepancy between our experimetally observed threshold and the theoretically predicted value is due to the sensitivity of the system to the modulation frequency. Numerical simulations of Eq. (4) predict that our 1% uncertainty in setting the driving

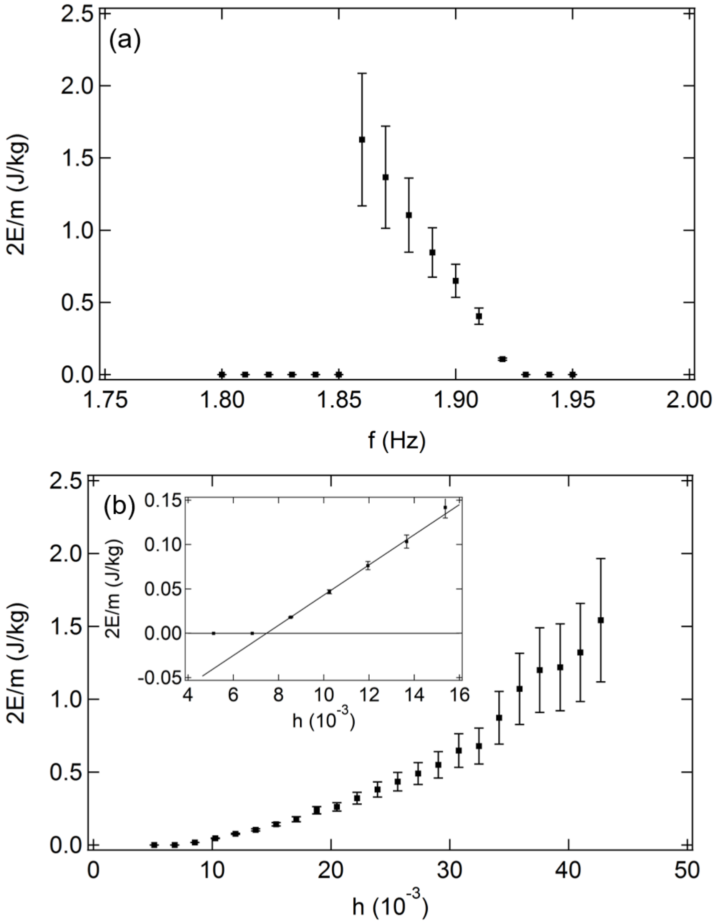

Figure 4. (a) Steady-state energy of the parametric amplifier at various modulation frequencies for a modulation depth of 0.031. (b) Steady-state energy of the parametric amplifier at various modulation depths, when the modulation frequency is twice the fundamental frequency, at 1.90 Hz. The inset graph shows the linear fit of the first few data points above the experimental threshold.

frequency can lead to the observed threshold increasing by a factor of 2.

Note also in Fig. 4 that the vertical error bars increase as a function of energy owing to the fact that the laser sensor records the passage time with an uncertainty of about 4 ms resulting in an increase in the uncertainty in the calculation of velocity and thus the energy as well. This uncertainty can be seen in the noise associated with the temporal plots in (Fig.3) near steady state.

We combine all the steady state energy data for various modulation frequencies and depths into one contour plot, as shown in Fig. 5. Here, the pendulum was driven in the neighborhood of the second-harmonic frequency. We observe the increase in the frequency range over which parametric oscillations build up as a function of modulation depth. The experimentally recorded minimum threshold modulation depth $h = 0.0085$ and an accurate value of the second-harmonic frequency $2f_0 = 1.90 \pm 0.02$ Hz for small amplitude are evident. The maximum recorded energy corresponds to the pendulum

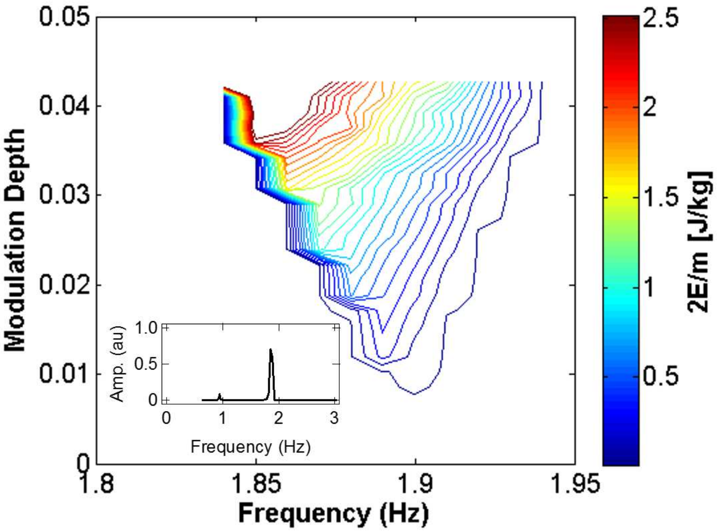

Figure 5. Contour plot of the steady-state energy of the parametric oscillator as functions of frequency and modulation depth. Zero energy is indicated by the solid black line. The inset graph shows the relative oscillation amplitude over a larger frequency span revealing a small amplitude at the fundamental frequency and a much larger amplitude for parametric driving.

oscillating with a maximum angular displacement of 80-90 degrees. As observed in Fig. 4(a), we see that the non-linearity of the system results in this peak energy to occur at a driving frequency of 1.84 Hz, 3% less than the second-harmonic frequency. The inset graph in Fig. 5 depicts the relative amplitude of the oscillator over a larger range of frequencies. Two resonances are observed, one weak resonance at the fundamental frequency of 0.95 Hz and a stronger resonance at the second harmonic frequency of 1.9 Hz. As obtained in the previous section, the lowest-order (and highest gain) parametric instability is observed when driving near the second harmonic. The weak resonance at the fundamental frequency corresponds to the next-lowest-order instability.

5. Bistability

We observe bistability in the steady-state energy of the system by increasing and then decreasing the modulation frequency through the parametric resonance. The data are shown in Fig. 6 where the steady state energy is plotted as a function of modulation frequency for several different modulation depths, h. We record passage time while increasing or decreasing the frequency in steps without pausing in-between steps. The inset in Fig. 6 indicates the sequence of measurements. We see that when the driving frequency increases the system is above threshold only near the parametric resonance. The frequency-increasing measurement is consistent with the data in Figs. 4(a)and 5.

When the driving frequency decreases through the parametric resonance, we observe that oscillations continue until a sudden drop-off occurs between $f = 1.6$ Hz and

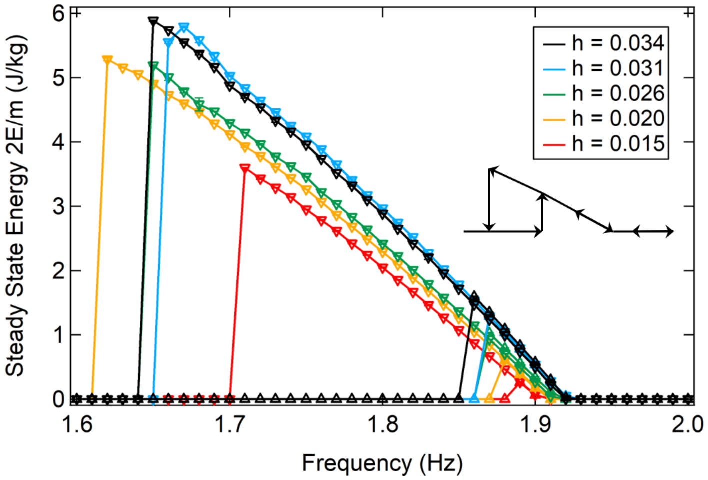

Figure 6. Bistability of the pendulum at various modulation depths. Each color represents one modulation depth. The upward-pointing triangles represent increasing frequencies, while the downward-pointing triangles indicate decreasing frequencies.

$f = 1.7$ Hz. The region in between 1.7 and 1.84 Hz exhibits two stable equilibrium states as expected for a nonlinear harmonic oscillator. The data also show that there is no obvious relationship between h and the frequency at which the system transitions back to the lower energy state. Simulations of the system using Eq. 4 also exhibit this transition frequency behavior. Within the simulation we can precisely set the initial position and momentum of the oscillator and we find that the steady state energy is sensitive to this setting. Experimentally we do not have precise control over the initial conditions of the oscillator because the change in modulation frequency happens randomly with respect to the position and speed of the oscillator.

6. Conclusion

We have described an intriguing and intuitive experiment which exhibits a parametric resonance. The pendulum can be constructed from components available in most instructional physics laboratories, and the driving mechanisms can be assembled from affordable motors and sensors combined with a programmable microcontroller. The scheme allows for the experiment to be interpreted with respect to the theory as presented in upper-division undergraduate physics textbooks in an elegant and quantitatively consistent manner. The experiment demonstrates chaotic properties allowing students to experimentally observe nonlinear dynamics. Moreover, a thorough understanding of this experiment provides a foundation for current research in quantum information and opto-mechanics where damped harmonic motion, Q, and parametric amplification are central.

References

[1] Baker GL and Blackburn JA 2005 *The Pendulum: a case study in physics* (Oxford: Oxford University Press).

[2] Taylor JR 2005,*Classical mechanics* (Sausalito: University Science Books) 457–520.

[3] Nation PD, Johansson JR, Blencowe MP, and Nori F 2012 *Rev. Mod. Phys.* **84** 1–24.

[4] Aspelmeyer M, Meystre P, and Schwab K 2012 *Phys. Today* **65** 29–35.

[5] Wollman E, Lei CU, Weinstein AJ, Suh J, Kronwald A, Marquardt F, Clerk AA, and Schwab KC 2015 *Science* **349** 952–955.

[6] Lecocq F, Clark JB, Simmonds RW, Aumentado J, and Teufel JD 2015 *Phys. Rev. X* **5** 041037–041045.

[7] Pirkkalainen JM, Damskägg E, Brandt M, Massel F, and Sillanpää MA 2015 *Phys. Rev. Lett.* **115** 243601–243606.

[8] Falk L 1979 *Am. J. Phys.* **47** 325-328.

[9] Case W 1980 *Am. J. Phys.* **48** 218–221.

[10] Case WB and Swanson MA 1990 *Am. J. Phys.* **58** 463–467.

[11] Berthet R, Petrosyan A, and Roman B 2002 *Am. J. Phys.* **70** 744–749.

[12] Curzon FL, Loke ALH, LeFrancois ME, and Novic, KE 1995 *Am. J. Phys.* **63** 132-136.

[13] Butikov EI 2004 *Eur. J. Phys.* **25** 535–554.

[14] Belyakov AO and Seyranian AP 2014 *Nonlinear Dyn.* **77** 1617–1627.

[15] Belyakov AO, Syranian AP, and Luongo A 2009 *Physica D.* **238** 1589–1597.